Sensors & Transducers, Vol. 226, Issue 10, October 2018, pp. 17-36

www.sensorsportal.com

Sensors & Transducers

Published by IFSA Publishing, S. L., 2018
http://www.sensorsportal.com

Laser Characteristics on Hard Tissue Laser Machining

[1, *] Gholamreza SHAYEGANRAD and [2] Leila MASHHADI

[1] Department of Biomedical Engineering, University of Basel, 4123 Allschwil, Switzerland
[2] Independent Researcher, Schweizergasse 28, 4054, Basel, Switzerland
[1] Tel.: +49-157-32930576, fax: +41-612-075409
[*] E-mail: gholamreza.shayeganrad@unibas.ch; shayeganrad@yahoo.com

Received: 25 June 2018 /Accepted: 31 August 2018 /Published: 31 October 2018

Abstract: Laser ablation of hard-tissue is coming today the most common medical application of the laser, mainly because of ability to cut faster, less invasive, and free incision geometry with a higher quality than the competing processes. Great efforts have been taken in the past to develop laser systems suitable for efficient laser ablation of hard-tissue. One of the drawbacks of the water-cooled laser-assisted bone cutting process is the limitation in incision depth. There are two main energy loss mechanisms which limit the achievable depth in addition to the absorption and scattering of laser energy by water. The first is the growing heat diffusion from the increasing surface area of the incision. The second is the increasing absorption and scattering of laser light by the ablation debris which is confined in deeper cuts. The desired specifications on the laser hard tissue ablation vary a lot in terms of laser parameters. In this paper, the influence of main laser parameters on water-cooled hard tissue laser ablation is reviewed. In particular, the role of the laser intensity, wavelength, duration of the laser pulse on depth of incision and mechanisms of photon energy transfer to biomedical materials are presented. In addition, the dependence of the ablation efficiency AE on the water content of the hard-tissue is presented. Finally, we presented a novel method that can bypass the limitation of the incision depth that can be introduced to laser osteotomy by long-pulsed mid-infrared lasers. In this technique an array of rotational micro-lens combined with a normal lens focuses the laser light on the bone tissue sample to increase the maximal incision depth.

Keywords: Er:YAG laser, CO2 laser, Er:YSGG laser, Micro-lens array, Thermo-mechanical ablation, Laser osteotomy, Incision depth.

1. Introduction

Bone machining such as drilling, cutting, slicing, sawing, milling, coring, and grinding are basic operations of orthopedics and trauma surgery. Using conventional tools like drills, saws, hammers, grinders, or burs osteotomes present significant limitations because of high mechanical load, high cutting temperature, poor accuracy, potential of damage to the surrounding tissues, high bleeding, and long operation time that make orthopedic surgery extremely complicated with the precision which is determined in part by the size and workspace of the tool. Indeed, undesirable physical or biological effects to the hard tissue apart from the material removal may result in severe mechanical trauma, long recovery and healing time, permanent impairment, pain and thermal damage to the adjacent remaining tissues [1-5]. Particularly, the main problem concerning hard bone tissue processing with invasive traditional orthopedic saws, blades or drills normally is generating substantial heat and raising temperature as well as non-smooth and non-precise cutting surface [1, 6]. In addition, the choice of incision geometry drastically limits to straight cuts or large radii of curvature.

Zhang, *et al.* [7] provided a comparison review on orthopedic surgery using piezosurgery and conventional tools. Although the state-of-the-art

piezo-osteotome has been applied increasingly in orthopedic surgery mainly because of its tissue selectively cutting function obtained by different frequencies as well as much more precision compared to the conventional tools, however, it still presents low-grade cut precision compared with laser-assisted hard bone tissue ablation. Cut edges show poor histological sharpness with irregular cut lines and poor incision quality with bone debris in the cut surface [8].

The need for clean, narrow, sharp, and precise cut geometry in orthopedic surgery lead lasers with various wavelengths have been evaluated continually. Such precision cuts are hard to achieve with conventional mechanical tools which normally induce mechanical stress, mechanical trauma, vibration, carbonization, and sometimes massive bleeding [9]. The rising temperature without cooling water increases with increasing laser fluency linearly and distributes into the surrounding tissues exponentially [10]. The water spray limits the temperature rises induced in the tissue to less than 3°C [10]. Lasers in the near-to mid-IR are eminently suitable for nondestructive hard tissue ablation in laser surgery. This is mainly due to very strong absorption of this functional wavelength regime by minerals (hydroxyapatite) as well as water in hard tissue, as shown in Fig. 1 [11]. The small amount of water presented in tissue absorbs laser energy strongly and vaporizes locally to generate enough pressure and ablate the tissue surface based on the thermomechanical ablation process.

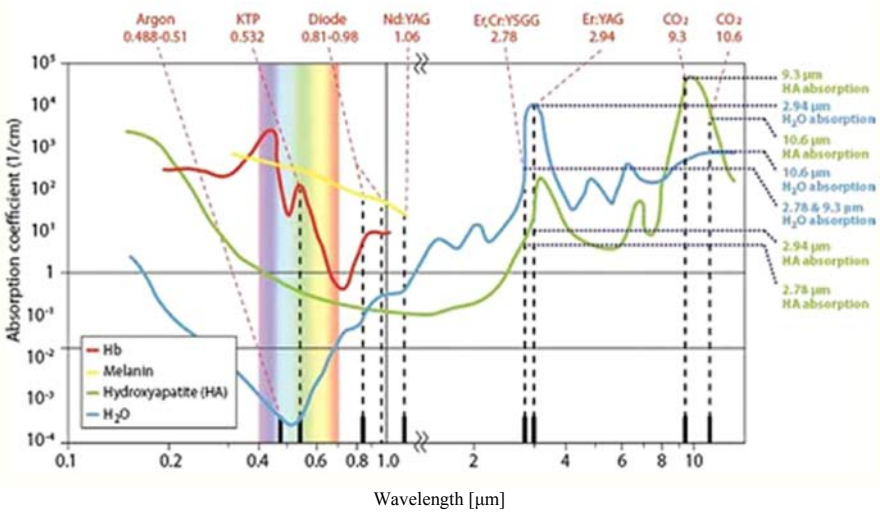


Fig. 1. Absorption spectra of various biological components [12].

The amount of water in the human body ranges from 50-75 %. Much of the water is in blood plasma (20 % of the whole body). According to a study performed by Mitchell [13], the amount of water in the human heart and brain is 73 %, the lungs are 83 %, the muscles and kidneys are 79 %, the skin is 64 %, and the bones are around 31 %. It is remarkable that the water percentage in different tissues and different organs of the body varies at different stages of growth [14]. The percentage of water in infants is much higher, typically around 75-78 % water, dropping to 65 % by one year of age. Fat tissue does not have water as much as lean tissue. Thus, people with more fatty tissue have less water than people with less fatty tissue (as a percentage). In adult women, fat makes up more of the body than men, so they have about 55 % of their bodies made of water; about few percent less than men, averaging around 50-65 % [15].

Although, non-contact laser surgery presents several advantages such as effectively less damaging surrounding tissue, less pain, less swelling, less bleeding, eliminating trauma, better cutting quality, and high accuracy [16], however, the cut depth saturates and the ablation efficiency drops with increasing incision depth [5]. This phenomenon is generally found in laser cutting of all kinds of materials. The trend is faster for Gaussian lasers with longer pulse width and smaller beam radius. There are two main energy loss mechanisms which limit the achievable depth in addition to the absorption and scattering of laser energy by water in water-assisted laser surgery. The first is the growing heat diffusion from the increasing surface area of the incision. The second is the absorption and scattering of laser light due to interaction of laser with the ejected ablation products (debris) which are more and more confined in the cut profile as the cut progresses deeper into the tissue and interact more and more even when pulse width is larger.

The first functional laser was invented by Maiman in 1960. It was a ruby laser in visible region (694.3 nm) which pumped by a xenon flashlamp. It was the first laser used in medicine in 1960 by Leon Goldman “father of laser medicine” tried to lighten tattoos by aiming a ruby laser at the pigmented skin until the pigment granules broke apart. In 1963

Charles Campbell used a ruby laser to treat a detached retina. In 1965 Goldman, *et al.* [17] and Stern and Sognnaes [18] introduced the first ruby laser in dentistry. Since then lasers are used in different medical applications i.e. osteotomy, surgery, lithotripsy, ontogenetic, cancer treatment, ophthalmology, dermatology, densitry, phlebology, and so on. In general, it is mostly because to their unique advantages, such as, contactless (sterile), vaporizational (coagulation) and precise (small focus diameter and wavelength-dependent penetration depth), methodology and good roughness [19-20]. In 1980s the Nd:YAG flashlamp pumped laser was developed. Soon after, novel laser diode pumped solid-stare lasers with different gain medium were constructed. So far, CW or pulsed solid-state laser from different crystals, mainly Nd^{3+} doped, such as Nd:YAG, Nd:YLF, Nd:YVO_4, (Er, Nd):YAG, (Ho, Nd):YAG, Nd:$GdVO_4$, Nd:LYSO, Nd:YAP, Nd:YAB, Nd:Mgo:$LiNbO_3$, Nd:GSAG, Nd:$LuVO_4$ Nd:$YAIO_3$, Er,Cr:YSGG, Er:YAG, Ti:sapphire, Yb:$KGD(WO_4)_2$ and Nd,La:SrF_2 with different laser emission wavelength has been demonstrated (see, for instance [21-30]). The active ion of Nd^{3+} has mainly three allowed transitions of $^4F_{3/2}\rightarrow{}^4I_{9/2}$, $^4F_{3/2}\rightarrow{}^4I_{11/2}$, and $^4F_{3/2}\rightarrow{}^4I_{13/2}$; corresponding to the emitting wavelengths around 0.9 μm, 1.06 μm, and 1.3 μm, respectively, makes it possible to achieve single- and multi-wavelength operations of an Nd^{3+} laser through a proper design of the laser. The capability of a laser can be extended by multiple wavelength engineered emission. The dual- or multi-wavelength simultaneously emission laser sources have been used in different scientific and technical applications in optical coherence tomography (OCT) [31-32], optical testing [33], atom interferometry [34], spectroscopy [35], THz radiation generation [36-37], and remote sensing [38-41].

The desired specifications of water-assisted hard tissue laser cutting vary a lot in terms of output power or fluence, wavelength, laser shape, pulse width, pulse shape, repetition rate frequency, etc. In order to perform minimally invasive medicine, it is important to optimize laser parameters such that laser cutting be fast, cuts being sharp and precise, the procedure be quiet with minimal vibrations imposed on the treated tissue, and the amount of residual heat that remains in the tissue following laser irradiation be also minimal. Up to now, the most promising laser sources for hard tissue ablation in mid-IR and IR spectral region, mainly because of very strong absorption, were found to be the CO_2 laser (9.6 μm and 10.6 μm), the Er:YAG laser (2.94 μm) and the Er,Cr:YSGG laser (2.78μm). CO_2 laser was developed first by Kumar Patel in 1964 at Bell Laboratories. As shown in Fig. 1, the wavelength of the Er:YAG laser at 2.94 μm coincides with the main spectral absorption peak of hydroxyapatite tissue and water [42-43]. This laser was first applied in dentistry. In contrast to many other lasers, the preparation of hard tissue like dentine, or enamel is possible with minimal thermal injury and higher cutting efficiency [9, 43-48].

The possibilities for using laser in dentistry did not occur until 1989, with the production of the American Dental Laser for commercial use [49]. This laser was an Nd:YAG laser, emitted pulses with width of approximately 100 μs, a maximum repetition rate of 30 Hz, and an maximum average output power of ~3 W. The great advance for dental lasers came in the mid-1990s with various laser types such as diode laser (810-890 nm), Nd:YAG (1064 nm), Er,Cr:YSGG, Er:YAG, and CO_2 becoming available to the dentists to address their needs for hard and soft tissue procedures [50-51]. Soft tissue laser ablation in near infrared (NIR) is characterized by a high absorption in chromophores (hemoglobin and melanin) found in soft tissue, resulting in excellent soft tissue incision, ablation and coagulation performance as well as antimicrobial effectiveness because of relatively deep and highly localized tissue heating. Whereas hard tissue laser ablation in mid-IR and infrared is characterized by a high absorption of hydroxyapatite and water in tissue.

In recent years, many studies have been carried out to evaluate the effects of Er:YAG laser irradiation with air jet, water jet, water mist or water spray on hard tissues laser ablation [10, 52-54]. In this paper, the effects of the main laser parameters on water-assisted hard tissue laser ablation are reviewed. In particular, the role of the intensity, wavelength, pulse width and repetition rate of the laser on depth of incision, ablation efficiency, and mechanisms of photon energy transfer to biomedical materials are presented. Water not only helps to remove debris from the ablation site and acts as a cooling agent, but also determines the ablation of tissues for thermomechanical effect by means of microexplosion of the water itself. In addition, the dependence of the ablation efficiency on the water content of the hard-tissue is presented. Finally, we proposed for the first time, to the best knowledge of authors, a novel technique that may bypass the limitation of the laser ablation in incision depth introduced to laser osteotomy by long-pulsed mid-IR lasers. In this technique an array of rotational micro-lens which is combined with a normal lens focuses the laser light on the hard tissue sample to increase the ablation efficiency in incision depth by creating channels in laser beam and reducing the effect of interaction laser and debris and therefore ejecting debris with less interaction with laser light. Consequently, the absorption and scattering of the incoming laser light by the debris decreases even with rising cut depth and thereby most of the energy can reach the depth of the incision.

2. Background

In two last decades, the remarkable progress in development of lasers with different wavelengths in the visible to far infrared region have gained laser application to various fields of medicine as standard instruments that are widely used in medical treatment and diagnostics. To better understand the special

advantages of lasers in biomedical field and effectively use them, the knowledge on radiation and biological tissues interaction and the chemistry of the tissues is essential. Indeed, it is important to know the mechanism of interaction induced by the laser radiation and where this process takes place within the tissue, in order to be able to avoid undesirable effects to the treated volume and surrounding tissues. In this section, the structure of hard tissues like bone and teeth is briefly presented. The interaction of laser with biological tissues, molecules and particles is also briefly discussed.

2.1. Bone Structure

Natural bone is a composite material composed of organic compounds (mainly collagen) reinforced with inorganic compounds (minerals). The inorganic component of bone is primarily crystalline hydroxyapatite, $Ca_{10}(PO_4)_6(OH)_2$ or HA. The crystals are platelets or rods, about 8-15Å thick, 20-40 Å wide and 200-400 Å long. Nanostructured HA are located discretely within the collagen fibers and thereby limiting the possible primary growth of the mineral crystals, and forcing the crystals to be discrete and discontinuous. Thereby the most prominent structures seen at nano-scale are the collagen fibers, surrounded and infiltrated by minerals. The detailed composition of bone differs depending on species, age, dietary history, health status and anatomical location. In general, about 70 % of the dry weight of bone consist of the inorganic compounds and the organic matrix makes up the remainder [55]. It means, around 30 % of bone is composed of organic compounds, of which 90 to 95 % is collagen, the rest being non-collagenous proteins. Collagen is a fibrous protein which provides the bone with strength and flexibility, and is an important component of many other tissues, including skin and tendon. Individual collagen molecules contain three polypeptides of about 1000 amino acids per chain with a high glycine and hydroxyproline content. The structure of the collagen molecule is stabilised by hydrogen bonds; the most common being between the amino group ($-NH_2$) of one residue and the carboxyl group (-COOH) of a second residue, resulting in both acidic and basic properties. Uncharged side-chains also interact with one another, but by excluding water from their mutual interfaces (i.e. hydrophobic reaction) [56].

The composed of the organic protein; collagen and the inorganic mineral hydroxyapatite provides a mechanical and supportive role in the body [57]. Depending on the orientation of collagen fibres, two types of bone can be distinguished, lamellar bone (cortical bone) and non-lamellar (trabecular or cancellous bone), which is found in vertebrae, at the ends of long bones, the mammalian foetus, at fracture joints, and in many lower vertebrates. Three types of cavities exit in bone; Haversian canals, marrow cavities, and the lacuna, which contain the bone cells (osteocytes) from which canalicuae (small tunnels) extend [58]. Collagen has an absorption spectrum almost similar that of HA, however, its absorption coefficient is about 3 orders of magnitude higher around 2.94 μm as shown in Fig. 2 [59].

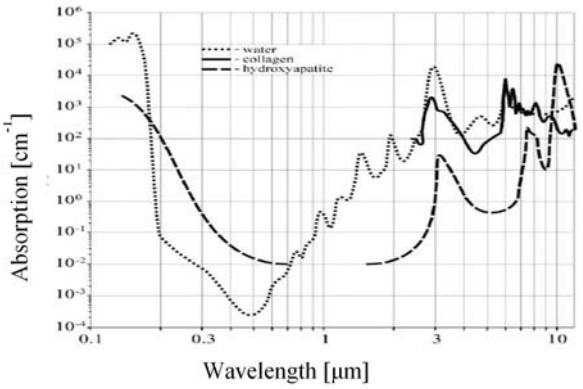


Fig. 2. The absorption spectra of water, collagen and hydroxyapatite [59].

2.2. Tooth Structure

The tooth is constructed of three layers; enamel, dentine, and pulp. Pulp cavity is the center part of the tooth that consists of blood vessels and nerves that enters the tooth from a hole at the bottom of the root. Pulp covered with the dentine where the tooth is exposed. Dentine is the inner and living tissue layer that lies beneath the enamel or cementum. Enamel is the outer calcified tissue layer covering the crown of the tooth. It is one of the hardest substances in the body. Cementum is the hard outer tissue layer covering the root and attaching the surrounding gum tissue to the root of the tooth. The cementum closely resembles cortical bone in composition, except that dentine is hard and dense, being almost 75 % weight mineral but with a higher collagen content than bone (30 % compared to 15 % in bone). The enamel is denser and harder and is almost 96 % mineral with the hydroxyapatite crystals being much larger than those of dentine, cementum or bone and consequently more resistant. Enamel has a very low intrinsic water content of 3 % weight in contrast to cementum with a relatively high intrinsic water content of 22 % weight. Dentin contains 12 % weight of water, bone contains approximately 22 % weight of water, and soft tissue contains 70 % weight of water [57, 60]. The water content of cementum is sufficient even for dry and efficient erbium laser ablation [61].

Table 1 summarizes composition of enamel and dentine as volume percent. The mineral in teeth is composed of a calcium-deficient carbonated hydroxyapatite ($Ca_{10-x}Na_x(PO_4)_{6-y}(CO_3)_z(OH)_{2-u}F_u$) in contrast to hydroxyapatite which has the formula $Ca_{10}(PO_4)_6(OH)_2$. These substitutions in the mineral crystal lattice, especially carbonate, renders tooth mineral more acid soluble than hydroxyapatite.

Table 1. Approximate composition of enamel and dentine at volume percent.

Component	Mineral	Water	Protein & lipid
Enamel	85	12	3
Dentine	47	20	33

2.3. Interaction of Laser with Biological Tissues

When a laser beam strikes on the surface of the tissue, a small fraction of the radiation is reflected according to the Fresnel equation and the remaining fraction is propagated into the tissue and undergoes absorption and scattering processes [62]. Intensity, wavelength, repetition rate, and duration of laser pulses are the most important parameters influencing the interaction of laser with molecules, particles and matters in macroscopic and microscopic scales.

The laser energy penetrates into the hard tissue depth (normally a few microns) depending on the absorption and scattering by tissue. The optical response of the tissue is given by the Beer-Lambert law:

$$F_\lambda(z) = (1-R)F_\lambda(0)\exp(-\mu_{eff}\, z), \qquad (1)$$

where $F_\lambda(z)$ is the laser fluence in the tissue [W/cm^2] at depth z and wavelength λ; F_λ (0) is the incident fluence [W/m^2] at wavelength λ; R is the Fresnel reflection coefficient, z is the penetration depth into the tissue [cm], $\mu_{eff} = \mu_a + \mu_s$ is the effective attenuation coefficient [cm^{-1}], where μ_a is absorption coefficient, and μ_s is scattering coefficient at the used wavelength. The absorption at wavelengths in the visible by biological tissues is mainly due to specific pigments of the tissue, such as hemoglobin in red blood cells, melanin in skin, and rhodopsin in the retina. However, in bone, absorption is introduced by collagen, water and hydroxyapatite nanocrystals.

Eq. (1) describes the exponential decrease of light fluence as a function of the material depth z due to the absorption and scattering processes: In the short range of penetration depth, the effective scattering coefficient is much smaller than the absorption coefficient ($\mu_s << \mu_a$) and therefor scattering by tissue is negligible. The depth at which the irradiance drops to the 1/e level is called optical penetration depth, $d=1/\mu_{eff}$. For instance, for compact human bone the penetration depth is limited to few microns in the mid-infrared spectral region near 3 μm due to strong absorption of water. It is remarkable that absorption and scattering by biological tissues may change during laser exposure. For instance, carbonization, in particular, may increase the absorption. However, the occurrence of carbonization must be avoided during any kind of clinical surgery.

For a biomedical tissue surrounded by air, the Fresnel equation is described as:

$$R = \frac{(1-n)^2 + k_{ext.}^2}{(1+n)^2 + k_{ext.}^2}, \qquad (2)$$

where n is the refractive index and $k_{ext.}$ is the extinction coefficient of the tissue. The absorption coefficient μ_a of the tissue can be connected to the extinction coefficient $k_{ext.}$ and wavelength λ by:

$$\mu_a = \frac{4\pi k_{ext.}}{\lambda} \qquad (3)$$

In general, absorption increases strongly by pulse duration and low intensity [63]. For polished human enamel, the reflectance at 9.6 μm and 10.6 μm has measured to be 49 % and 13 %, respectively, while human dentin reflects 17 % and 9 % at 9.6 μm and 10.6 μm, respectively [64]. For hydroxyapatite ($n \approx 1.530$ and $k_{ext.} \approx 8\times10^{-3}$) surrounded by air (n=1), the power reflectance at normal incidence can be obtained to be about 4 %.

Laser is used every day, for instance, to remove unwanted tattoos, make incisions during surgeries, and treat aches and pains. Each of these applications works because of one of the types of laser-tissue interactions: photothermal, photomechanical, photoablation, plasma-mediated ablation, or photochemical that depends on the irradiation time and laser intensity as well (see Fig. 3) [62].

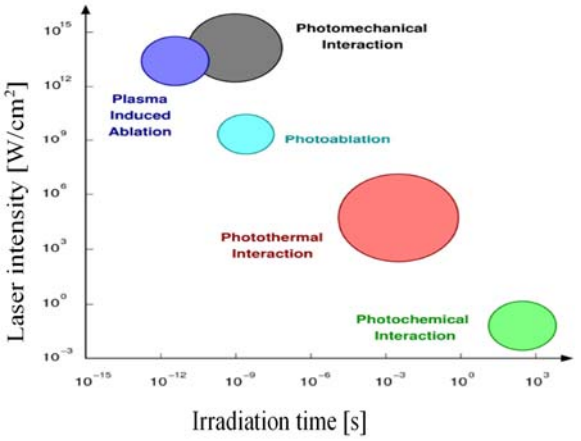


Fig. 3. Types of laser-tissue interactions.

2.3.1. Photothermal

Ultrashort pulses (<10 ps) have been shown to generate little thermal or mechanical damage. In general, thermal effects can be decreased by reducing the pulse duration [65-66] or by using lasers with radiation wavelength in the UV range [67-68]. Lasers that produce a photothermal effect use prolonged energy exposure to facilitate an increase in chromophore temperature, which in turn leads to cellular vaporization. This type of laser-tissue interaction is what occurs during surgical, ablation,

and hair removal using laser. The absorbed energy by biological tissue converts to heat. Thermal effects can be induced by either CW or pulsed laser radiation. This may lead to distortion or the destruction of a tissue volume. In biological tissues, absorption is mainly caused by either water molecules or macromolecules such as proteins and pigments. For instance, water strongly absorbs the Er:YAG wavelength at 2.94 μm and thus water within the layer of tissue vaporizes to induce localized micro-explosions. Liquid water is a collection of polar molecules connected by hydrogen bonds. When water transfers from liquid to vapor, it expands quit a lot and therefore induces increase in pressure. The density of liquid water is approximately 0.96 gr/cm^3 at 100 ^{o}C and atmospheric pressure. The density of water vapor at 100 ^{o}C and atmospheric pressure is about a factor of 1600 less, and therefore water expands by a factor of 1600 when it turns into vapor at atmospheric pressure.

Depending on the duration and peak value of the temperature of tissue, different effects like coagulation, vaporization, carbonization, and melting may be distinguished. Fig. 4 shows a scheme of the thermal interaction in biological tissues for different temperatures. During the process of coagulation, temperature reach at least 60 ^{o}C At temperatures between 50 °C and 100 °C occurs the denaturation of the biomolecules and their aggregates (proteins, collagen, lipids, and hemoglobin) or irreversible coagulation of proteins. When the temperature of the tissue reaches about 100 °C the water constituting most of the tissues vaporizes to dehydrate the tissue. When the presented water in the tissue is completely evaporated, the tissue temperature rapidly increases up to about 300 °C and the tissue burns. At this point, increasing the deposition energy on the tissue, carbonization may occur. In this case, the local temperature of the exposed tissue drastically increases. Actually, at temperatures above approximately 100 ^{o}C, the tissue starts to carbonize, leading to a blackening in color. For medical laser applications, carbonization should be avoided in any cases. Increasing temperature may lead to melt the tissue. For instance, if the temperature reach a few hundred degree Celsius, tooth substance which mainly consist of hydroxyapatite, a chemical compound of calcium and phosphate starts melting. The pulse duration of a few microseconds is sufficient enough to enable an increase in temperature.

It is possible to control the temperature rise and limiting thermal damages to the predetermined target to minimize the spread of heat to adjacent tissues. A high heating causes an irreversible deformation of biological tissues and losing of protein function. In situations when a laser pulse width is shorter than thermal relaxation time of the tissue (e.g. delivering short laser pulses), the initial temperature distribution assuming no heat conduction can be given by [69]:

$$\Delta T(z) = \frac{\mu_a Q_0 e^{-\mu_a z}}{\rho c A}, \quad (4)$$

where $\Delta T(z)$ [^{o}C] represents the one-dimensional temperature distribution, z is the depth [cm], A is the area [cm^2], c is specific heat [mJ/gr.^{o}C], ρ is density of the tissue [gr/cm^3], and Q_o is the incident energy [mJ].

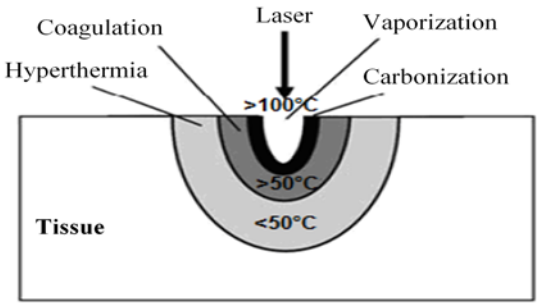


Fig. 4. Scheme of the thermal interaction in biological tissue for different temperatures.

2.3.2. Photomechanical

The photomechanical effects are obtained with lasers emitting extremely short pulses, in the nanosecond to picosecond range on very small surfaces, which causes a destructive shockwave mainly induced by the mechanism of explosive vaporization of the target. These waves then break up the target material into smaller particles, making it useful for applications such as tattoo removal, photo refractive keratectomy, and treat haemangiomas. In the last case, the vessels of the angioma explode. This is also what happens during a tattoo removal when large fragments of pigment explode and give birth to smaller fragments.

2.3.3. Photoablation

Photoablation is an efficient, highly precise and flexible tool being used for a growing number of medical applications. Photoablation consists in the spontaneous etching that occurs upon the absorption of a pulse of laser at the material surface. Strong absorptions of most of the biomolecules in UV and visible involve a localized molecular dissociation that can be accompanied by thermal effects or not, leads of evaporation and ionization with the formation of plasma and removal of material from the tissue. The laser ablation starts when the laser intensity exceeds certain threshold values that allow the removal of material from the irradiated target, requires high power density (10^7-10^{10} W/cm^2) and pulse durations ranging typically from 10 ns to 100 ns.

Biological tissues can also be etched or cut beautifully with a high lateral and depth resolution laser photoablation. Photoablation is the most recent light-tissue interaction to be exploited in microsurgery such as keratoplasty, angioplasty, and neurosurgery. The advantage of using UV light resides in the fact that the ablation is strictly confined to the volume that absorbs the energy. The presence of water, which is

essentially non-absorbing in UV, does not affect significantly the cleanliness of the photoablative cut by UV laser. Nevertheless, the threshold of ablation is increased by wavelength (100 mJ/cm^2 at 193 and 500 mJ/cm^2 at 248 nm for the cornea tissue). Due to high absorption coefficient in UV of many materials, the laser energy is very densely absorbed at the surface and therefore ablation volume is very small. UV laser Photoablation has an advantage which does not damage the tissue.

UV lasers are used in LASIK (laser in situ keratomileusis) eye surgery. Commonly used excimer molecules include fluorine (emitting at 157 nm) and noble gas compounds (Argon-193 nm, Krypton-222 nm, etc.). The femtosecond laser is the new scalpel for biologists. Since 2000, the surgeons have gradually become familiar with this tool, which opens up great prospects in life sciences [70-71].

CO_2 lasers with wavelengths centered around 10 μm and represent a cost effective alternative to UV lasers. Unlike UV lasers, IR laser ablation is a purely thermal process. The laser beam directly applies heat on the tissue which partially evaporates. They typically produce a clean cut structure, thanks to high absorbance in IR by hard tissues.

The photoablation rate (AR) can be assumed to be proportional to the difference between the laser fluence F and the threshold fluence F_{th}:

$$AR = k(Fe^{-\mu_a z} - F_{th}), \quad (5)$$

where μ_a is the effective absorption coefficient, and k is the rate constant. Photoablation will take place if $F>F_{th}$. The ablation depth d, i.e. the depth at which $F(z) = F_{th}$, should then be [62]:

$$d \simeq \frac{1}{\mu_a} \ln \frac{F_0}{F_{th}} \quad (6)$$

It shows ablation depth increases logarithmic with laser fluence. Above the threshold of plasma generation, F_{pl}, the ablation depth per pulse saturates due to the well-known phenomenon called plasma shielding. Thereby, all abundant energy dissipates to heat leading to additional thermal effects by means of nonradiative relaxation. Hence, the crucial parameter for differentiating photoablation and thermal interaction is the photon energy or laser wavelength.

For a Gaussian spatial beam profile with a $1/e^2$-beam radius (w_0), the measured diameters ($D = 2r_a$) of the ablated areas are related to the threshold fluence F_{th} [72]

$$F_{th} = F_0 \exp(-2r_a^2 / w_0^2), \quad (7)$$

where F_0 is the applied peak laser fluence. For laser pulses with a Gaussian spatial beam profile, the maximum irradiation fluence F can be calculated from the irradiation pulse energy E_p and the beam radius w_0:

$$F_0 = 2E_p / \pi w_0^2 \quad (8)$$

From Eq. (7), if the fluence F exceeds the ablation threshold fluence F_{th}, the squared diameters of the ablated area of the ablation crater is correlated as [73]:

$$D^2 = 2w_0^2 \ln(F_0 / F_{th}) \quad (9)$$

Substituting Eq. (8) into Eq. (9), we can obtain:

$$D^2 = A\ln(E_p) + B, \quad (10)$$

where

$$A = 2w_0^2, \quad (11)$$

$$B = \pi w_0^2 \ln(2 / \pi w_0^2 F_{th}) \quad (12)$$

Eqs. (10)-(12) show that the ablation threshold fluence and the radius of the laser beam waist could be calculated from fit parameters to squared diameter of the ablated areas and the corresponding incident laser pulse energy.

The depths of the ablated features such as holes or grooves can be very difficult to estimate. Different methods such as probe sensing [74], optical profilometry [75], coated replicas [76], profile observation [77], tomography [78], and differential weighing method [79] employed for estimation the depth. Weighing clearly enables faster determination of such phenomenological parameters without any methodological issue compared to the other methods. The ablation volume ΔV can be deduced as:

$$\Delta V = \frac{\Delta m}{\rho}, \quad (13)$$

where ρ is the volume density of the tissue. The higher the ablated mass is, the more accurate the ablated rate is. The ablated mass Δm can be adjusted by changing the number of pulses during laser ablation. The volume ablation rate τ_{vol} being the ablated volume per pulse, can be used to calculate the number of pulses N_p which were used to ablate the tissue. In the static case (micro cavity and drilling), N_p can be easily determined by operator. In the dynamic case (cutting), effective number of pulses can be calculated from [80]:

$$N_p = \sqrt{\frac{\pi}{2}} \frac{f.L_{tot}}{v}, \quad (14)$$

where f is the repetition rate of the laser, v is the velocity of the translation stage, and L_{tot} is the total length of cut.

The ablated volume per number of pulses being calculated, the exact volume ablation rate τ_{tot} can be determined by [79]:

$$\tau_{tot} = \frac{\Delta V}{N_p} = \frac{\Delta m.v}{\rho.f.L_{tot}} \quad (15)$$

2.3.4. Plasma-mediated Ablation

Plasma-mediated ablation makes use of high energy laser pulses to ionize molecules with the first few femtosecond of the pulses and induced nonlinear absorption. This process leads to ablate the tissues in sub-micrometer size with negligible heat damage to the surrounding tissues. When the laser intensity exceeds 10^{13}-10^{14} W/cm^2 corresponding an electric field of ~10^8-10^9 V/cm in the order of electric field of the bind electrons in molecules, ablation proceeds via ionizing molecules at the focus and producing bubble of plasma at the focus with a high concentration of electrons and ions. This intensity can be achieved, for instance, with 100 nJ, 100 fs pulses focused into 1 μm^2 area.

In general, the interaction between a femtosecond laser and biological tissue takes place via "plasma-mediated ablation."[81]. The generated free electrons by either multiphoton absorption or tunneling ionization, accelerate by inverse-Bremsstrahlung absorption, in which electrons absorb photons while colliding with molecules, or by laser electric field. After achieving sufficient energy to ionize another molecules, the density of plasma increases and eventually limits the penetration of the incident pulses to the skin depth of only few nanometers. Following shielding, free electrons recombines with the positively ionized molecules and transfers their energy to the molecules in a time scale which is shorter than ~100 ps acoustic relaxation time in materials. Consequently, a dramatic increasing pressure within the excitation volume can produces rupture and form cavitation. The expansion of the cavitation is associated with an acoustic shockwave that propagates into the surrounding tissues and has potential of spreading damage.

The most important aspect is that the laser pulse is significantly shorter than the time it takes for electrons to transfer their energy to the lattice via electron-phonon coupling. The laser-induced plasma then absorbs the laser energy very quickly, causing the rapid removal, or ablation, of the target tissue with negligible thermal issues.

The ablation threshold is affected by the laser pulse width, wavelength and pulse numbers, among other factors, and was reported to be 0.6-2.2 J/cm^2 for enamel and 0.3-1.4 J/cm^2 for dentin (see, e.g. [82-83] and reference therein). For multiple pulse ablation, the decrease of the ablation threshold with an increasing number of pulses was observed. When a low laser fluence was applied, only a small proportion in the center of the laser spot could cause ablation. However, when the laser fluence is increased far beyond the ablation threshold (F_{th}), a "plasma shielding" effect may take place. Lizerelli, *et al.* [84] observed a conventional ablation pattern with photo thermal effect for enamel using femtosecond laser with central wavelength of 800 nm and fluence of 13 J/cm^2 corresponding intensity of ~1.8×10^{14} W/cm^2. In this case, only part of the energy was enough to cause the ablation process. However, with a laser fluence of 32 J/cm^2 and average intensity of 191 mW, a sharp edge or rim definition preserving the original characteristics of the enamel and a highly prismatic structure was observed [84]. In this case that the pulse width is of 70 fs less than the vibration relaxation time of the crystalline net (photon relaxation time) of the enamel, is of 100 fs, there is no time for the energy dissipation to the lattice via electron-phonon coupling or heat.

2.3.5. Photochemical

Lasers using photochemical effects do not destroy or break up tissue. Light that interacts with tissue in a photochemical manner is absorbed into the chromophores and precipitates a biological cascade of events that promotes pain relief and inflammation reduction. Photochemical laser-tissue interactions are operative in therapy applications, such as deep tissue laser therapy (DTLT) and photodynamic therapy (PDT). Photochemical interaction mechanisms play a significant role during PDT. Today, the idea of PDT using photosensitizer, e.g. hematoporphyrin derivative (HpD), has become one of the major pillars in the modern tumor treatment

Photochemical interactions take place at very low power densities (typically 1W/cm^2) and long exposure times ranging from seconds to CW [62]. The laser parameter can be selected such that the laser radiation penetrates the tissue. In most cases, wavelengths in the visible range are used because of their high optical penetration depth. For instance, the relative low absorption at approximately 620–630 nm is used for clinical purposes where deeper structures can be reached due to the lower absorption coefficient of most tissues in the red spectrum.

2.4. Interaction Laser with Molecules and Particles

The laser light interacts with the molecules and particles via a multitude of phenomena such as elastic scattering (molecular-Rayleigh, aerosol-Mie), inelastic scattering (molecular–Raman, particle-breakdown), fluorescence, and absorption [85]. Scattering leads to decrease the transmitted energy similar to absorption. It refers to the processes in which photons change direction after an interaction. The intensity of scattered light depends on some parameters such as wavelength and intensity of incidence light as well as density, shape and size of the scatters. Rayleigh and Mie scattering scatters the photon in a different direction to its incoming direction without a change in photon energy. Rayleigh scattering is observed from particles with dimension smaller than the light wavelength. The Rayleigh scattering cross section (cm^2) is obtained as [86]:

$$\sigma_R = 4.577\times10^{-21}\frac{\delta}{\lambda^4}\left[A(1+B/\lambda^2)\right]^2, \qquad (16)$$

where λ [in μm] is the wavelngth, and $\delta = (6+3\Delta)/(6-7\Delta)$ with the depolarization factor Δ. Coefficients values of A, B, and δ are summarized in Table 2 for various molecules.

Table 2. Coefficients for computing the Rayleigh scattering cross-section.

Molecule	A(×10^{-5})	B(×10^{-3})	δ
N_2	29.06	7.70	1.05
Ar	29.06	7.70	1.00
CO_2	43.9	6.4	1.15
air	28.71	5.67	1.06

For a mixture gases, the Rayleigh scattering cross-section can be obtained from:

$$\sigma_R = \sum_m \sigma_{Rm} n_m , \qquad (17)$$

where n_m is the mixing ratio by volume, of molecules m. The Rayleigh scattering cross-section for a CO_2 molecule is depicted in Fig. 5 as a function of wavelength. Rayleigh scattering by molecules is important for wavelengths up to 1.0 μm, The Rayleigh scattering cross-section decreases rapidly with wavelength, and then this trend becomes flatter and is not significantly sensitive to wavelength.

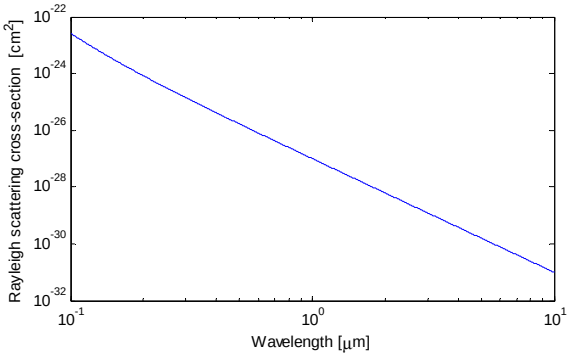


Fig. 5. Rayleigh scattering cross-section as a function of wavelength.

On the other hand, in the presence of particles with size of the order or larger than the incident light wavelength, such as a water droplet or debris, the Mie scattering becomes predominant. For large particles, forward Mie scattering is more probable than backward-direction scattering. Mie scattering efficiency is generally much bigger than the Rayleigh's one. In hard tissue laser ablation, debris range in size from a few tenths of nanometer to about a hundred micrometers. For a fixed wavelength, the attenuation due to molecular scattering is smaller than that of aerosol scattering. In other words, the Mie scattering losses can be much larger than the Rayleigh scattering losses if enough particles are presented, especially for large wavelengths.

The absorption and scattering coefficients of water sprays (i.e. cloud of non-uniform size water droplets) can be predicted with Mie scattering theory. The theory allows one to calculate absorption, scattering and extinction efficiency function of homogenous particles (droplets) in terms of non-dimensional size parameter χ (=2πr/λ) and complex index of reflection n´=n(λ)+ik(λ), where r is the radius of a scattering spherical particle, and λ=λ$_0$/n is wavelength. Rayleigh scattering, Mie scattering, or Geometric scattering is dominant, when χ<<1, χ~1, or χ>>1, respectively. The scattering regimes for a single scattering sphere particle in ultraviolet, visible, and infrared regions is shown in Fig. 6.

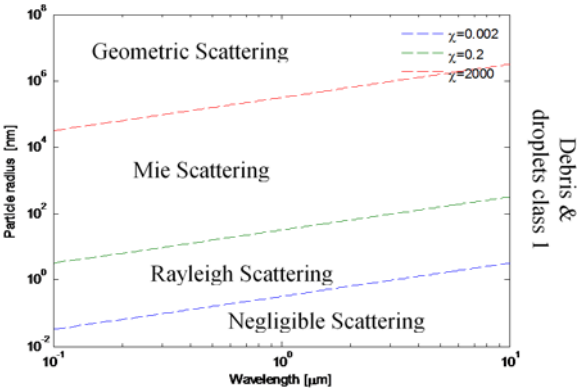


Fig. 6. The scattering regimes for a single scattering sphere particle. For details refer to the text.

Assuming that the particles have the same optical properties, the Mie total scattering cross section is expressed as the infinite series [87]:

$$\sigma_M = \left(\frac{2\pi}{k^2}\right)\sum_{n=1}^{\infty}(2n+1)(|a_n|^2 + |b_n|^2), \qquad (18)$$

where k=2π/λ. The coefficients a_n and b_n are given by:

$$a_n = \frac{\mu m^2 j_n(mx)[xj_n(x)]' - \mu_1 j_n(x)[mxj_n(mx)]'}{\mu m^2 j_n(mx)[xh_n^{(1)}(x)]' - \mu_1 h_n^{(1)}(x)[mxj_n(mx)]'}, \qquad (19)$$

$$b_n = \frac{\mu_1 j_n(mx)[xj_n(x)]' - \mu j_n(x)[mxj_n(mx)]'}{\mu_1 j_n(mx)[xh_n^{(1)}(x)]' - \mu_1 h_n^{(1)}(x)[mxj_n(mx)]'}, \qquad (20)$$

where the j_n's are spherical Bessel functions of the first kind, the h_n's are spherical Hankel functions, and μ_1 and μ are the magnetic permeability of the sphere and surrounding medium, respectively. m=n_{sph} /n_{med} is the ratio of the refractive index of the particle to that of the surrounding medium. The series expression converges after a number of terms slightly larger than the size parameter. The normalized scattering cross-section,

$\sigma/\pi r^2$, versus size parameter, χ, is shown in Fig. 7. The cross-section oscillators in the Mie scattering region and its maximum amplitude places at χ=1. The oscillation is because of constructively and destructively interference of wave that reflects directly from the frond surface of the sphere and creeping wave that travels around the back of the sphere. The corresponding Mie scattering cross-section is more complex than Rayleigh scattering with wavelength dependence proportional to λ^{-x}, where 0.4<x<0.5.

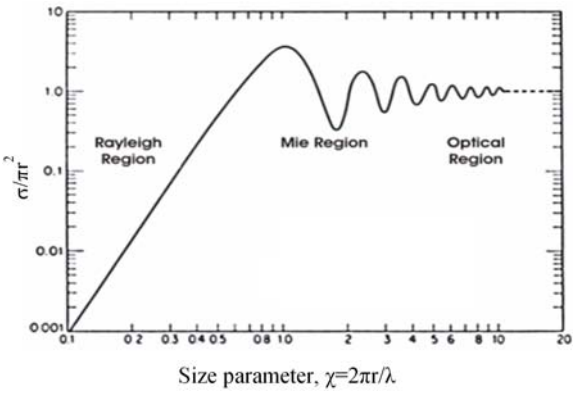


Fig. 7. Normalized scattering cross-section versus size parameter, χ [88].

Generally, water is not opaque but semitransparent to radiation. However, for wavelengths greater than 2 μm water becomes strongly absorbing, and large droplets are expected to be opaque to incident radiation for λ>2 μm. Water sprays are of non-uniform size and the droplet size distribution depends on the design of the nozzles, water pressure for producing the water spray and the operation conditions. According to the size of the droplets, it can be divided to class 1, 0≤d≤200 μm, class 2, 200<d≤500 μm, class 3, 400<d<1000 μm in diameter.

The spectral absorption varies in different types of materials. Absorption spectrum of CO_2 and H_2O in ultraviolet, visible, and infrared regions are compared in Fig. 8. Carbon dioxide has three large absorption bands in the infrared region at about 2.7 μm, 4.3 μm, and 15 μm. Water has several absorption bands in the infrared, and even has some absorption well into the microwave region.

3. Influencing Parameters on Hard Tissue Laser Ablation

As mentioned above, the desired specifications of laser-assisted hard tissue cutting vary a lot in terms of output power, wavelength, laser shape, pulse width, repetition rate frequency, etc. In order to perform highly efficient minimal invasive laser surgery and protecting over-heating surrounding tissues, it is important to optimize laser parameters such that laser cutting be fast, cuts being sharp and precise, the procedure be quiet with minimal vibrations imposed on the treated tissue, and the amount of residual heat that remains in the tissue following laser irradiation being also minimal.

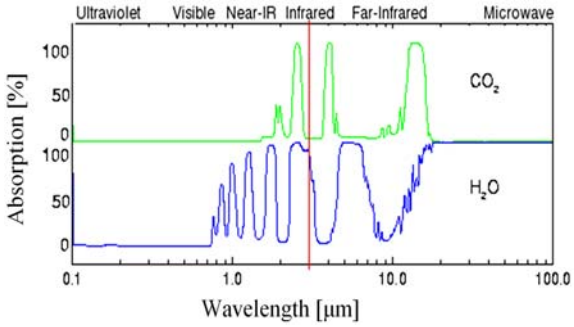


Fig. 8. Absorption spectrum of CO_2 and H_2O in UV to IR regions. (Data from refs. [89-90], original data are from Howare, *et al.* [91] and Goody [92].

3.1. Laser Pulse Shape and Incidence Angle

Assuming a super-Gaussian beam energy profile, the following equation applies:

$$F(r) = F_0 \exp\left[-2(r / w_0)^{2N}\right], \quad (21)$$

where F is the fluence at a radial distance r of the axis of the laser beam, F_0 is the peak fluence (at the axis of the laser beam), w_0 is the laser beam size, and N is the super-Gaussian order of the beam profile. N=1 represents a pure Gaussian beam profile, and N→∞ represents a flat-top beam profile.

Similar obtaining Eq. (9) for a pure Gaussian beam, the squared diameters of the ablated area of the ablation crater is correlated as [93-94]

$$D^2 = 4w_0^2 \left[\frac{1}{2}\ln\left(\frac{F_0}{F_{th}}\right)\right]^{1/N}, \quad (22)$$

The depth of ablation given by Eq. (6) can be modified for non-normal incidence as [93-94]:

$$d \simeq \frac{1}{\mu_a}\ln\left(\frac{F_0 \cos\theta}{F_{th}}\right), \quad (23)$$

where θ is the incidence angle. The squared diameter given in Eq. (22) is modified to Eq. (24) for non-normal incidence angle [93-94]:

$$D^2 = \frac{4w_0^2}{(\cos\theta)^2}\left[\frac{1}{2}\ln\left(\frac{F_0 \cos\theta}{F_{th}}\right)\right]^{1/N}, \quad (24)$$

For non-normal incidence the spot area of ablation impact is given by [93-94]

$$A = \frac{4\pi w_0^2}{(\cos\theta)^2}\left[\frac{1}{4}\ln\left(\frac{F_0}{F_{th}}\right)\ln\left(\frac{F_0\cos\theta}{F_{th}}\right)\right]^{1/2N}, \quad (25)$$

The volume of ablation impact for non-normal incidence can be calculated as [93-94]:

$$V = \frac{\pi w_0^2}{\mu_a 2^{1/N}}\left[\ln\left(\frac{F_0}{F_{th}}\right)\right]^{1/N} \times\left[\frac{N}{N+1}\ln\left(\frac{F_0}{F_{th}}\right)+\ln(\cos\theta)\right], \quad (26)$$

The optimum spot depth at non-normal incidence can be calculated from Eq. (23) when

$$F_{0,opt} = \frac{F_{th}}{\cos\theta}e, \quad (27)$$

which results

$$d_{opt} = \frac{1}{\mu_a}, \quad (28)$$

The optimum spot diameter at non-normal incidence can be obtained from Eq. (24) to result:

$$D = \frac{2w_0}{\cos\theta}\left[\frac{1}{4N}\right]^{1/2N}, \quad (29)$$

The optimum spot area at non-normal incidence can be calculated from Eq. (25) to obtain:

$$A = \frac{\pi w_0^2}{\cos\theta}\left[\frac{1}{2N}\right]^{1/N}, \quad (30)$$

The optimum spot volume at non-normal incidence can be calculated from Eq. (25) to obtain:

$$V = \frac{\pi w_0^2}{\mu_a 2^{1/N}}\left[\frac{N+1}{N}-\ln(\cos\theta)\right]^{1/N} \times\left\{1+\ln\left[(\cos\theta)^{1/(N+1)}\right]\right\}, \quad (31)$$

3.2. Laser Wavelength

Wavelength is a key factor in the suitability of any laser for hard-tissue procedures in dentistry and osteotomy. Over the last forty years, the most promising laser sources for hard tissue ablation in the infrared spectral region were found to be the CO_2 laser (9.6 μm & 10.6 μm), the Er:YAG laser (2.94 μm) and the Er:YSGG laser (2.78 μm). The Er:YAG and the Er,Cr:YSGG lasers make up the erbium family of dental lasers. When comparing the wavelengths of the erbium doped lasers, the Er:YAG laser's wavelength of 2.94 μm matches the absorption peak of water at 2.94 μm (12000 cm^{-1}) while the absorption coefficient of water for the 2.78 μm (4000 cm^{-1}) wavelength is 3 times lower (see Fig. 9). The difference in the absorption coefficients leads to a difference in the penetration depth in hard tissues.

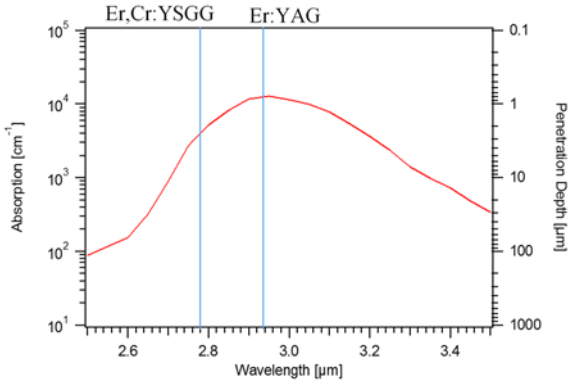


Fig. 9. The absorption curve of water in the middle infrared region. The blue lines show the position Er,Cr:YSGG and Er:YAG lasers. Replotted data from [95].

In the case of relatively large penetration depth, the laser energy may spread out to the surrounding tissues by the process of thermal diffusion before absorption laser energy sufficiently and reach the explosion point that is necessary in thermomechanical ablation process. In other words, the higher the penetration depth, the longer the time required to reach the explosion temperature. For effective ablation hard tissues with minimal thermal side-effects, it is important that the ablation process takes place over a short time so that very little heat is transferred to the surrounding tissues [96-97]. Fig. 10 shows that the ablation efficiency of Er:YAG for hard tissue ablation is higher compared to that of Er,Cr:YSGG (see [98] and reference therein). The absorption coefficients of enamel and dentin at 2.94 μm is 1500 cm^{-1} and 2000 cm^{-1}, respectively.

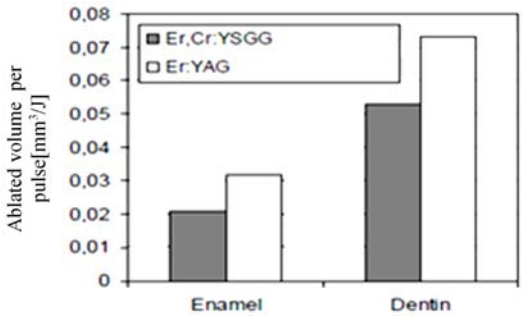


Fig. 10. Ablated volume per pulse energy of dentine and enamel for different laser wavelengths both laser sources at 260 mJ pulse energy [98].

In contrast to the Er:YAG and Er,Cr:YSGG lasers which operate in the region of the major water absorption, CO_2 and Ho:YAG lasers show

significantly lower absorption in water and are thus less suited for treatments in this field. Comparison of the measured ablation speed (mm^3/s) for Er:YAG and Er,Cr:YSGG laser shows that ablation speed of dentine and enamel increases linearly with fluence and the ablation speed of hard tissue with Er:YAG is always larger compare to that of the Er,Cr:YSGG.

3.3. Laser Fluence and Pule Width

Dependence of the ablation threshold in enamel and dentin on the pulse duration and laser type is shown in Fig. 11. The ablation threshold for the shortest SSP (50 μs) Er:YAG laser pulse is by a factor of 3 lower compared to that of the H (500-700 μs) Er,Cr:YSGG laser pulse, and by a factor of 6 lower compared to the S (1600-2000 μs) Er,Cr:YSGG laser pulse. As expected, ablation threshold increases towards longer pulse durations.

The effect of fluence on ablation diameter is shown in Fig. 12. It can be seen that D^2 varies linearly with $\ln(E_p)$, where E_p is energy per, to approve Eq. (9). In this experiment the beam waist radius (w_0) was ~15 μm and the ablation thresholds (F_{th}) of dentin and enamel were 1.18 and 1.38 J/cm^2, respectively. The laser emitted a Gaussian beam with a wavelength of 1.025 μm, pulse width of 400 fs, repetition frequency of 30 to 200 kHz, and average power up to 4 W.

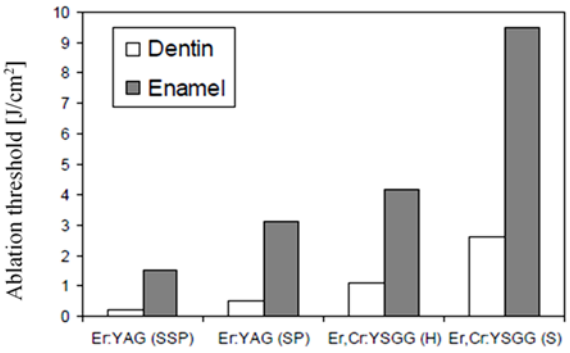


Fig. 11. Dependence of the ablation threshold in enamel and dentin on the pulse duration and laser wavelength [98].

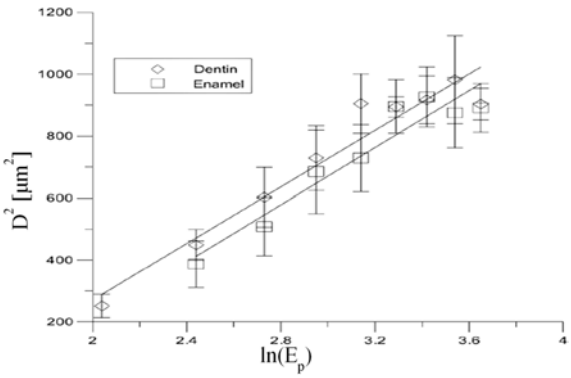


Fig. 12. The squared diameters of the ablated area for dentin and enamel versus natural logarithm of E_p [82].

Ultrashort pulses (<10 ps) have been shown to generate little thermal or mechanical damage. Thermal effects can be decreased by reducing the pulse duration [65-66] or by using lasers with radiation wavelength in the UV range [67-68]. Ablation rate of enamel and dentin as a function of laser fluence with 350-fs and 1-ns pulses show a clear pattern of saturation near 3 J/cm^2 for both enamel and dentin. With 350-fs pulses, ablation threshold for dentin was at 0.5 J/cm^2 and for enamel at 0.7 J/cm^2 [66]. In contrast, ablation threshold for dentin with the longer, 1-ns pulses of 1050 nm was about 20 J/cm^2. A rapid exponential drop in ablation efficiency with increasing fluence was also observed with 350-fs pulses for both enamel and dentin with a slightly higher efficiency for dentine [66].

Enamel and dentin were also ablated with a 66 fs laser pulses at a wavelength of 800 nm and a repetition rate of 1 kHz [82]. The focal spot of the laser was ~100 μm. The initial temperature of the pulpal chamber was 23.6°C. During the laser ablation process, the temperature rose to a peak value of 35.9°C (ΔT = 12.3°C). Following the addition of air cooling, the temperature dropped to 26.6°C (ΔT = 3.0°C). At a laser fluence of 11 J/cm^2 and a scanning velocity of 1 mm/s, the ablation rates of enamel and dentin were measured to be 5.7×10^{-3} mm^3/s and 56.0×10^{-3} mm^3/s, respectively. According to [82], the ablation efficiency initially increases almost linearly and then deceases, suggesting that it is possible to find an appropriate fluence value to achieve a maximum ablation efficiency (see Fig. 13). Maximum ablation efficiency of dentin 0.019 mm^3/J is about 2 times of maximum ablation efficiency of enamel 0.009 mm^3/J. Decreasing ablation efficiency is due to the plasma shielding. Taking into account the maximum ablation efficiency of enamel and 300 mm^3 of dental hard tissue, mostly enamel, that is ground out during tooth preparation for a typical full metal crown of a molar, a femtosecond laser with an average power of ~18 W is required to complete the tooth preparation work within half an hour.

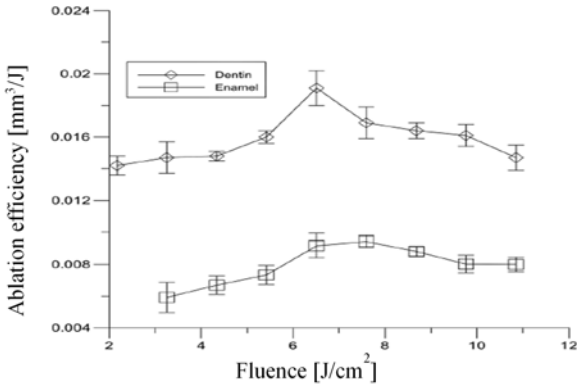


Fig. 13. The ablation efficiency of the ablated area of dentin and enamel versus fluence with a 66 fs laser pulses at a wavelength of 800 nm and a repetition rate of 1 kHz [82].

It is known that the ablation threshold decreases towards shorter pulse durations [98-100]. This is due to the fact that for shorter times, the energy has little time to escape from the irradiated volume to the surrounding tissues by heat diffusion to result in faster ablation and smaller amount of residual heat deposition. Fig. 14 shows ablation depths of drilled into dentin (top) and enamel (bottom) with ten consecutive Er:YAG at 2.94 μm laser pulses of different duration [96]. With pulse lengths of 100 μs and 300 μs, the ablation of dentine starts abruptly at a well-defined fluence value of 4.0±0.5 J/cm^2.Within the experimental error, the ablation threshold is independent of the pulse duration. At higher fluences, the ablation depths increase quasi-logarithmically as a result of absorption and scattering of the laser beam by the ejected debris. The ablation depths of drilled into enamel show qualitatively the same behavior as that in dentin. At the pulse length of 100 μs, they follow a quasi-logarithmical functional dependence on the applied laser fluence, as predicted by the debris screening model, except for the fluences above 50–70 J/cm^2 where increasingly deeper craters are obtained.

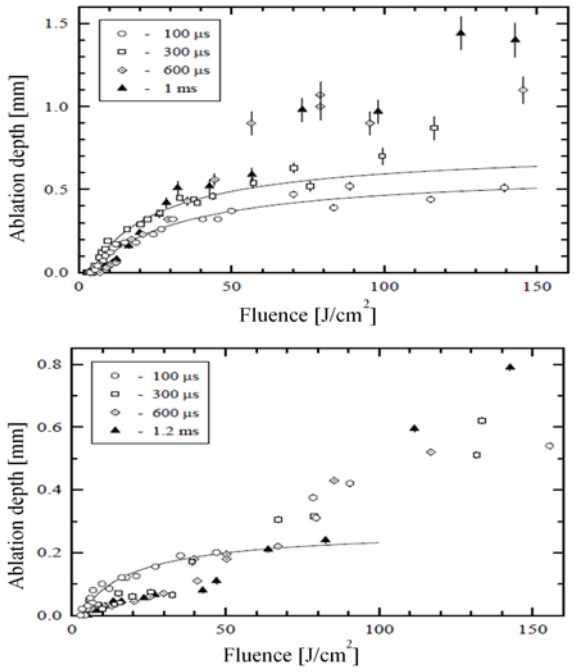


Fig. 14. Ablation depths of drilled into dentin (top) and enamel (bottom) with ten consecutive Er:YAG at 2.94 μm laser pulses of different duration (see [96] for details).

3.4. Water Cooling

The influence of external cooling on the temperature rise in the tooth pulpal chamber during femtosecond laser ablation was investigated. The ablation were performed on dentin using an Yb:KYW which generates a Gaussian 1030-nm radiation wavelength beam with 560-fs pulse duration [101]. The experiments were performed in air and with surface cooling by a lateral air jet and a combination of an air jet and water irrigation. The ablation rate versus fluence for different cooling methods is plotted in Fig. 15. Independently of the cooling method used, the ablation rate increases linearly with fluence in the range of 2–14 J/cm^2. External cooling has a negligible influence on the ablation rate for fluences in the tested fluence range with fs laser pulses.

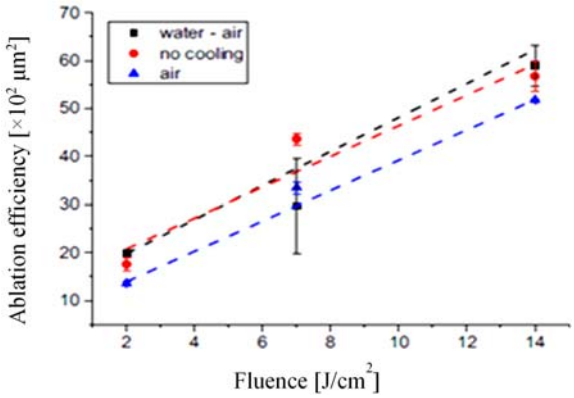


Fig. 15. Ablation rate versus fluence for different cooling methods with 1030-nm laser wavelength and 560-fs [101].

The temporal behavior of the pulpal chamber temperature during a laser treatment without external cooling, with an average fluence of 7 J/cm^2 and a pulse repetition rate of 1 kHz, is depicted in Fig. 16 [101]. It can be seen that temperature initially increases to reach maximum 34.5°C after 65 s, and then remains approximately constant during the full duration up to the end of the laser treatment (175 s). After stopping the laser, the temperature drops almost exponentially with the quiet slow cooling rate due to the low thermal diffusivity of dentin.

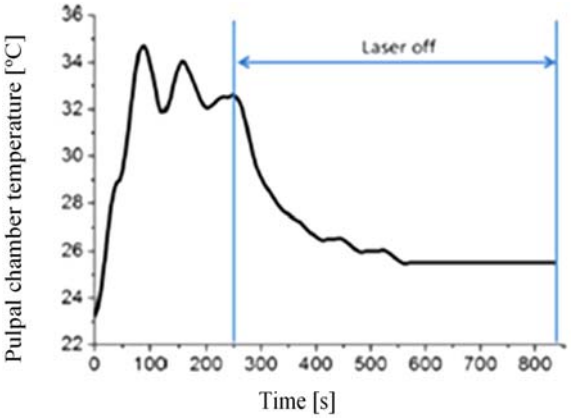


Fig. 16. Dynamic behavior of the pulpal temperature during femtosecond laser irradiation with 7 J/cm^2 [101].

The temperature increases with fluence from approximately 3.1°C for 2 J/cm^2 to 17.5°C for

14 J/cm^2 (Fig. 17). The temperature rise reached 17.5°C for the treatments performed with 14 J/cm^2 and without cooling, which was reduced to 10.8 ± 1.0 and 6.6 ± 2.3°C with forced air cooling and water cooling, respectively, without significant reduction of the ablation rate.

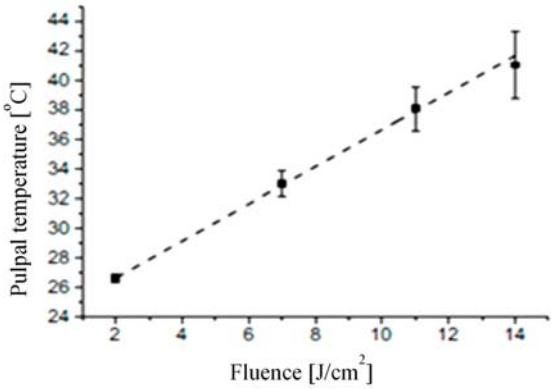


Fig. 17. Maximum temperature of pulpal versus fluence [101].

In addition, the effect of pulse duration on, the ablated dentin by Er:YAG laser at 1 Hz with a fixed energy at 150 mJ/pulse corresponding to fluence ~113 mJ/pulse for three seconds with a water spray (water: 17.6 ml/min; air: 1.2l ml/min) has been reported in [51]. As the pulse duration increased, the ablated dentin became deeper but the diameter thereof decreased. Fig. 18 shows the depths of the cavities after laser irradiation with various pulse durations. As the pulse duration of Er: YAG laser increased, depth of the cavities increased.

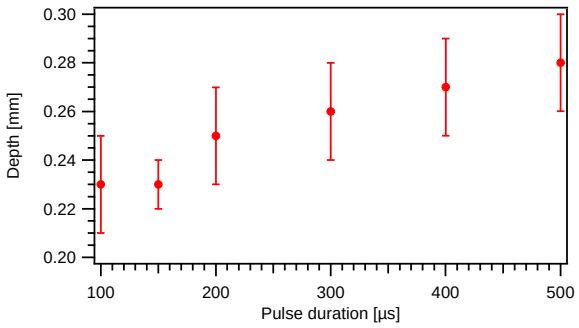


Fig. 18. Depths of ablated dentin after laser irradiation. Reproduced from [51].

Fig. 19 shows variation of diameter of the cavities after laser irradiation versus pulse duration. The longer the pulse duration of Er:YAG laser, the smaller the diameter of the irradiated spot.

As shown in Fig. 20, volume of the cavities did not change statistically with the pulse duration of Er:YAG laser. The average cavity volume following [51] is given by:

$$V = \pi r^2 \frac{d}{3} \tag{32}$$

is plotted in Fig. 20 [51].

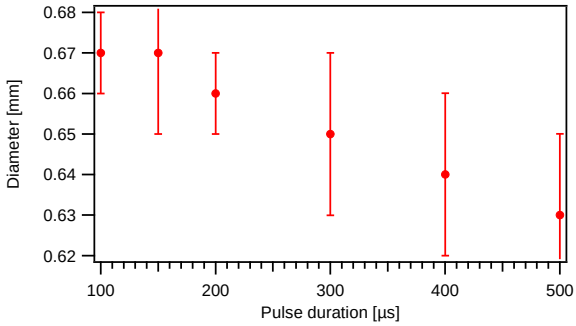


Fig. 19. Diameters of ablated dentin after laser irradiation as a function pulse duration. Reproduced from [51].

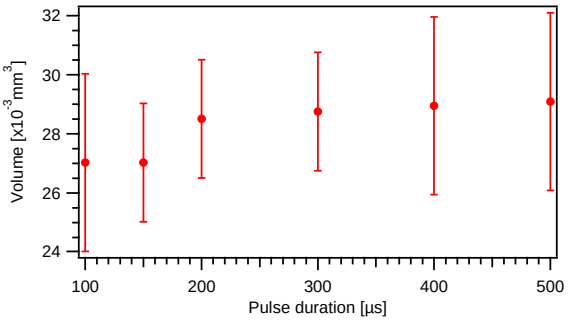


Fig. 20. Estimated volumes of ablated dentin after laser irradiation. Reproduced from [51].

Remarkably different methods have been proposed and investigated for remote monitoring incision depth in laser surgery [102]. Pulsed laser ablation results in vaporization and ejection of tissues, leading to generation of laser-induced shockwaves at the incision spot.

On the other hand, recently Kuščer and Diaci [61] measured precisely erbium laser-ablation efficiency in hard dental tissues under different water cooling conditions. In enamel, the highest AE, with clean cavities and no signs of thermal damage, was observed under the "pores" conditions when the superficial dental tissue was rehydrated only during the time in-between laser pulses. However, when in addition to the rehydration in-between the pulses, the pulsed laser beam was intersect with water-spray particles above the tooth ("spray" conditions), or with a water layer on the tooth surface ("pool" conditions), resulted in a reduction of AE.

The effect of pulse duration on reduction of AE has been also investigated [61]. It was found that spray functions only as an absorber and not as an enhancer of the AE and this effects gains for longer pulse durations. This can be explained by noting that during longer pulse durations more water is delivered to the

tooth, and therefore, more laser energy is required to sustain the vapor tunnel [61]. The relative decrease in AE due to the presence of spray versus pores, D_{spray}, as a function of Er:YAG pulse duration is depicted in Fig. 21. As expected, an approximately linear dependence of D_{spray} on the pulse duration and consequently on the amount of water delivered during the duration of each laser pulse is obtained (see [61] for details).

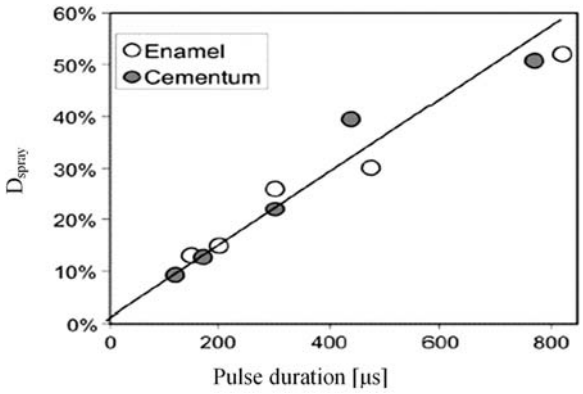


Fig. 21. Relative reduction in AE, D_{spray}, in enamel and in cementum as a function of Er:YAG pulse duration [61].

6. Reducing Debris Effect

It was already known that the interaction of laser light with ejected debris has a considerable influence on ablation characteristics of erbium lasers [103]. By using a quantum square pulse (QSP) chopped pulse Er:YAG mode (see Fig. 22) which was designed to reduce the temporal crossing of incoming laser radiation with ejected debris, it was possible to significantly increase dental enamel and cementum ablation drilling efficacy and reduce the rate of tissue desiccation. The appropriately timed chopped pulse structure of the QSP mode was shown to result in a high cutting efficacy and low thermal side-effects, a characteristic of short pulses, and in low vibrations and sharp cuts, which is a characteristic of longer pulses [103].

Ablation saturation was observed for all measured laser modes with the depth d_{sat} depending on the laser pulse duration (see Fig. 23). The ablation saturation depth was measured to be largest for the QSP mode and decreases with increasing laser pulse duration.

Although the ablation saturation depth and ablation efficiency was measured to be largest for the QSP mode, but chopper wheel which modulates the laser beam blocks the laser light and therefore reduces the ablation rate with decreasing energy per pulse. An alternative method to reduce the temporal cross-over of incoming laser radiation with ejected debris is combination of rotational micro-lens array with a normal lens (see Fig. 24) which focuses the laser light on the hard tissue sample. The rotation velocity defines by distance between microlenses in array, velocity of ejection of debris and depth:

$$\omega = \frac{l.v}{R.d}, \tag{33}$$

where l is the distance between microlenses, R is the distance of microlenses from center of the array, ω is the angular frequency, and v is the average of ejection velocity of debris. In this method, debris can be ejected from the cannels generated by lenslet without interaction with laser beam.

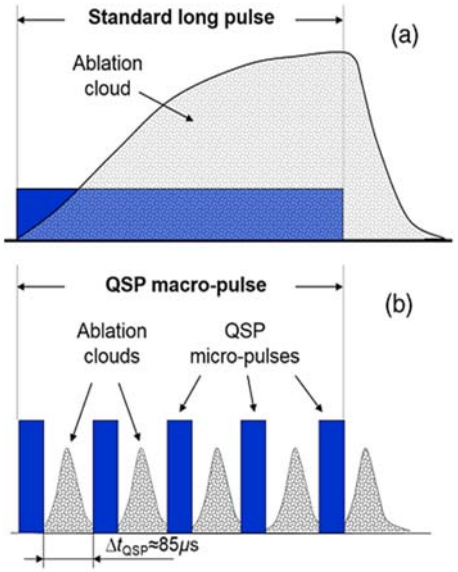


Fig. 22. a) Standard laser pulse; (b) QSP laser pulse. A 600-μs macropulse is chopped into five micropulses with duration of t_{QSP}= 50 μs, and temporal spacing between the micropulses of Δt_{QSP}=85 μs [103].

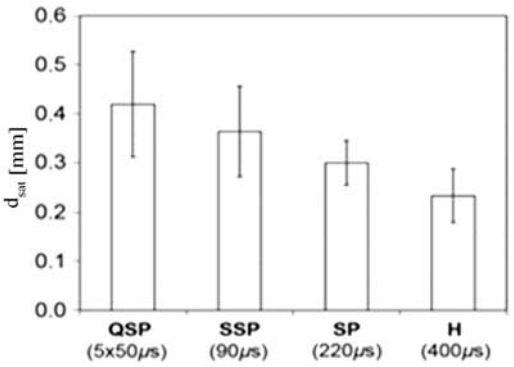


Fig. 23. Dependence of the ablation saturation depth (d_{sat}) in enamel for different erbium laser pulse modes [103].

7. Conclusions

Nowadays, only a few studies have investigated the difference between laser surgery and conventional tools, and the influence of laser parameters are not fully understood, especially in depth of incision. By analyzing literature relevant to laser surgery and conventional tools during surgery research in vivo and

in vitro, the influence of laser parameters on water-cooled hard tissue laser ablation and depth of incision is reviewed.

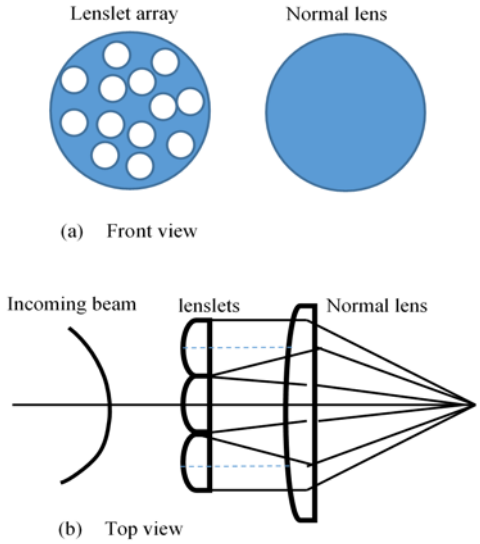


Fig. 24. (a) Front view, and (b) top view of combination of rotational micro-lens with a normal lens to reduce the temporal crossing of incoming laser radiation and ejected debris in hard-tissue laser ablation.

The characteristic of hard tissue machining comprising conventional surgical instruments can be affected by the surgery parameters such as cutting force or pressure, cutting rate, cutting speed, cutting temperature, bone surface, bone damage, bone thickness, cutting efficiency and so on. For piezosurgery, in addition to these parameters, ultrasonic properties such as frequency and amplitude as well as tip structure, and bone density are also relevant during surgery.

Non-contact laser surgery presents several advantages such as effectively less damaging surrounding tissue, less pain, less swelling, less bleeding, eliminating trauma, better cutting quality, and high accuracy. However, the cut depth saturates and the ablation efficiency drops with increasing incision depth which depends on laser parameters. This phenomenon is generally found in laser cutting of all kinds of materials. The trend is faster for Gaussian lasers with longer pulse width and smaller beam radius. There are two main energy loss mechanisms which limit the achievable depth in addition to the absorption and scattering of laser energy by water. The first is the growing heat diffusion from the increasing surface area of the incision. The second is the absorption and scattering of laser light due to interaction of laser with the ejected ablation products (debris) which are more and more confined in the cut profile as the cut progresses deeper into the tissue and interact more and more when pulse width is larger.

Wavelength is a key factor in the suitability of any laser for hard-tissue procedures in dentistry and osteotomy. So far, the most promising laser sources for hard tissue ablation in the infrared spectral region were found to be the CO_2 laser (9.6 μm & 10.6 μm), the Er:YAG laser (2.94 μm) and the Er:YSGG laser (2.78 μm). The Er:YAG and the Er,Cr:YSGG lasers make up the erbium family of dental lasers. When comparing the wavelengths of the erbium doped lasers, the Er:YAG laser's wavelength of 2.94 μm matches the absorption peak of water at 2.94 μm (12000 cm^{-1}) while the absorption coefficient of water for the 2.78 μm (4000 cm^{-1}) wavelength is 3 times lower. The difference in the absorption coefficients leads to a difference in the penetration depth in hard tissues.

Er:YAG lasers are currently in use for dental hard tissue ablation in clinical practice. Ablation is accomplished through the localized laser-induced generation of heat, an example of the photothermal effect. However, as the pulse width of the laser is increased, the thermal effect becomes more obvious, producing significant collateral damage in the target area (e.g., microcracking, carbonation and melting).

Femtosecond lasers, unlike Er:YAG lasers, use ultrashort pulses. When the pulse width is shorter than the target material's thermal relaxation time, thermal diffusion cannot take place, and strong peak power can ionize the material into plasma, thus greatly reducing the generation of thermal effects and collateral damage. Indeed, cold ablation processing can be attained with high accuracy and almost no effect on the vitality of the pulp. When the excitation time is shorter than the thermalization time in the material, non-thermal, photochemical ablation mechanisms can occur. It induces a clean ablation of tissue without thermal effects.

Ablation thresholds decrease toward shorter pulse durations, where short pulses are pulses shorter than the thermal relaxation time of the ablated tissue In general, thermal effects can be decreased by reducing the pulse duration or by using lasers with radiation wavelength in the UV range. At shorter times, the energy has little time to escape from the ablated volume, and so less heat is diffused into the surrounding tissue. Lasers that produce a photothermal effect use prolonged energy exposure to facilitate an increase in chromophore temperature, which in turn leads to cellular vaporization. This type of laser-tissue interaction is what occurs during surgical, ablation, and hair removal with laser. Shorter pulses, therefore, result in faster ablation and smaller amount of residual heat deposition. On the other hand, short laser pulses are expected to produce higher-frequency tissue vibrations and may therefore cause more discomfort to patients.

At short pulse durations, strong absorption of incoming laser beam by dense debris cloud above the irritated area results a reduced ablation rate. The scattering effect caused by the debris cloud leads to spreading out the laser beam and therefore less precise the cut geometry. The laser reheats the debris and it falls back to the tissue surface to additional heating the tissue and consequently reducing the ablation rate and additional residual heat deposition.

A quantum square pulse (QSP) chopped long pulses in NIR region makes it possible to significantly increase dental enamel and cementum ablation drilling efficacy and reduce the rate of tissue desiccation with decreasing temporal crossing of incoming laser radiation and ejected debris. However, chopper wheel blocks the laser light to result modulation of laser beam with the expense of energy loss. An alternative novel method to reduce the temporal cross-over of incoming laser radiation with ejected debris is combination of rotational micro-lens with a normal lens which focuses the laser light on the bone tissue sample. In this method an array of rotational micro-lens which is combined with a normal lens focuses the laser light on the hard tissue sample to increase the ablation efficiency in incision depth by creating channels in laser beam and reducing the effect of interaction laser and debris and therefore ejecting debris with less interaction with laser light. Consequently, the absorption and scattering of the incoming laser light by the debris decreases even with rising cut depth and thereby most of the energy can reach the depth of the incision.

References

[1]. A. R. Eriksson, T. Albrektsson, B. Albrekisson, Heat caused by drilling cortical bone, *Acta Orthop. Scand*, Vol. 55, Issue 6, 1984, pp. 629-631.

[2]. P. D. Gabrić, *et al*., Comparison of Er:YAG Laser and Surgical Drill for Osteotomy in Oral Surgery: An Experimental Study, *J Oral Maxillofac Surg*, Vol. 70, Issue 11, 2012, pp. 2515-2521.

[3]. A. Troedhan, *et al*., Cutting bone with drills, burs, lasers and piezotomes: A comprehensive systematic review and recommendations for the clinician, *Int. J. Oral Craniofac Sci*, Vol. 3, Issue 2, 2017, pp. 020-033.

[4]. S. Toksvig-Larsen, L. Ryd, A. Lindstrand, Temperature influence in different orthopaedic saw blades, *J. Arthroplasty*, Vol. 7, Issue 1, 1992, pp. 21-24.

[5]. G. Shayeganrad, L. Beltran, G. Rauter, P. C. Cattin, A. Zam, Effects of laser parameters on incision depth of bone ablation in laser osteotomy, in *Proceedings of the 1st International Conference on Optics, Photonics and Lasers (OPAL'18)*, Castelldefels, Barcelona, Spain,
9-11 May 2018, pp. 40-41.

[6]. S. Toksvig-Larsen, L. Ryd, A. Lindstrand, Temperature influence in different orthopaedic saw blades, *J. Arthroplasty*, Vol. 7, Issue 1, 1992, pp. 21-24.

[7]. Y. Zhang, C. Wang, S. Zhoua, W. Jiang, Z. Liu, L. Xu, A comparison review on orthopedic surgery using piezosurgery and conventional tools, *Procedia CIR*, 2017, Vol. 65, pp. 99-104.

[8]. U. Romeo, A. D. Tenore, P. Visca, C. Maggiore, Bone damage induced by different cutting instruments: an in vitro study, *Braz Dent J*., Vol. 20, Issue 2, 2009, pp. 162-168.

[9]. M. Frentzen, W. Goetz., M. Ivanenko, S. Afilal, M. Werner, P. Hering, Osteotomy with 80 μs CO_2 laser pulses—histological results, *Laser Med. Sci*., Vol. 18, 2003, pp. 110-124.

[10]. S. R. Visuri, J. T. Walsh, H. A. Wigdor, Erbium Laser Ablation of Dental Hard Tissue: Effect of Water Cooling, *Lasers in Surgery and Medicine*, Vol. 18, Issue 3, 1996, pp. 294-300.

[11]. A. Vogel, V. Venugopalen, Mechanisms of pulsed laser ablation of biological tissues, *Chem. Rev*., Vol. 103, Issue 2, 2003, pp. 577–644.

[12]. D. Fantarella, L. Kotlow, The 9.3-μm CO_2 Dental Laser: Technical Development and Early Clinical Experiences, *J. Laser Dent*., Vol. 22, Issue 1, 2014, pp. 10-27.

[13]. H. H. Mitchell, T. S. Hamilton, F. R. Steggerda, H. W. Bean, The chemical composition of the adult human body and its bearing on the biochemistry of growth, *J. Biol. Chem*., Vol. 158, 1945, pp. 625-637.

[14]. R. M. Forbes, A. R. Cooper, H. H. Mitchell, The composition of the adult human body as determined by chemical analysis, *J. Biol. Chem*., Vol. 203, 1953, pp. 359-366.

[15]. https://water.usgs.gov/edu/propertyyou.html.

[16]. R. J. Wallace, C. J. Whitters, J. A. McGeough, A. Muir, Experimental evaluation of laser cutting of bone, *J. of Materials Processing Techno*logy, Vol. 149, 2004, pp. 557–560.

[17]. L. Goldman, J. A. Gray, J. Goldman, B. Goldman, R. Meyer, Effects of laser impacts on teeth, *J. Am. Dent. Assoc*., Vol. 70, 1965, pp. 601–606.

[18]. Stern R. H., Sognnaes R. F., Laser beam on dental hard tissues, *J. Dent. Res*., Vol. 43, 1964, pp. 873.

[19]. L. Högberg, S. Reinius, S. Stahle, K. Vogel, G. Wallin, Laser microsurgery upon the inner ear and myelinated nerves, in Vestibular function on earth and in space, in *Proceedings of the Wenner-Gren Center International Symposium Series*, Vol. 15, 1970, pp. 159-170.

[20]. T. Oshiro, The CO_2 laser as an ideal microsurgical tool, *Lasers Surg Med*., Vol. 6, Issue 1, 1986, pp. 29-37.

[21]. G. Shayeganrad, Y.-C. Huang., L. Mashhadi, Tunable single and multiwavelength continuous-wave c-cut Nd:YVO4 laser, *Appl. Phys. B*, Vol. 108, 2012, pp. 67–72.

[22]. G. Shayeganrad, L. Mashhadi, Dual-wavelength CW diode-end-pumped a-cut Nd:YVO4 laser at 1064.5 and 1085.5 nm, *Appl. Phys. B*, Vol. 111, Issue 2, 2012, pp. 189–194.

[23]. G. Shayeganrad, Actively Q-switched Nd:YVO4 dual-wavelength stimulated Raman laser at 1178.9 nm and 1199.9 nm, *Opt. Commun*., Vol. 292, 2013, pp. 131–134.

[24]. C. W. Luo, Y. Q.Yang, I. T. Mak, Y. H. Chang, K. H. Wu, T. Kobayashi, A widely tunable dual-wavelength CW Ti:sapphire laser with collinear output, *Opt. Express*, 2008, Vol. 16, Issue 5, pp. 3305-3309.

[25]. Z. Qin, *et al.,* Femtosecond and Dual-Wavelength Picosecond Operations of Nd,La:SrF2 Disordered Crystal Laser, *IEEE Photonics Journal*, Vol. 9, Issue 2, 2017, p. 1502007.

[26]. W. Li, Q. Hao, J. Ding, H. Zeng, Continuous-wave multi-wavelength diode-pumped Yb:GYSO laser, *J. Opt A Pure Appl Opt*, Vol. 10, Issue 9, 2008, p. 095307.

[27]. C.Y. Li, Y. Bo, J. L. Xu, C.Y. Tian, Q. J. Peng, D. F. Cui, Z. Y. Xu, Simultaneous dual-wavelength oscillation at 1116 and 1123 nm of Nd:YAG laser, *Opt. Commun*., Vol. 284, Issue 19, 2011, pp. 4574–4576.

[28]. A. Brenier, Tunable THz frequency difference from a diode-pumped dual-wavelength Yb3+:KGd$(WO_4)_2$

laser with chirped volume Bragg gratings, *Laser Phys, Lett.*, Vol. 8, 2011, pp. 520–524.

[29]. B. Xu, Y. Wang, Y. Cheng, Z. Lin, H. Xu, Z. Cai, R. Moncorgé, Diode-Pumped CW Laser Operation of a c-cut Nd:YAlO3 Crystal on Low-Gain Emission Lines Around 1.1 um, *IEEE Photonics Journal*, Vol. 7, 2015, p. 1503407.

[30]. G. Shayeganrad, Tunable single- and dual-wavelength nanosecond Ti:Sapphire laser around 765 nm, *Appl. Phys. B*, Vol. 124, Issue 8, 2018.

[31]. Y. Mao, S. Chang, E. Murdock, C. Flueraru, Simultaneous dual-wavelength-band common-path swept-source optical coherence tomography with single polygon mirror scanner, *Opt. Lett.*, Vol. 36, Issue 11, 2011, pp. 1990–1992.

[32]. S. Chang, Y. Mao, C. Flueraru, Dual-Source Swept-Source Optical Coherence Tomography Reconstructed on Integrated Spectrum, *International Journal of Optics*, Vol. 2012, 2012, p. 565823.

[33]. A. García-Arellano, F. Granadis-Aquestin, M. Campos-García, A. Cornejo-Rodríguez, Ronchi test with equivalent wavelength, *Appl. Optics*, Vol. 51, Issue 15, 2012, pp. 3071–3080.

[34]. V. Ménoret, R. Geiger, G. Stern, N. Zahzam, B. Battelier, A. Bresson, A. Landragin, P. Bouyer, Dual-wavelength laser source for onboard atom interferometry, *Opt. Lett.*, Vol. 36, Issue 21, 2011, pp. 4128–4130.

[35]. S. Shibata, Dual-Wavelength Spectrophotometry. *Angew. Chem. Int. Ed. Engl.*, Vol. 15, Issue 11, 1976, pp. 673–679.

[36]. A. Saha, A. Ray, S. Mukhopadhyay, N. Sinha, P. K. Datta, Simultaneous multi-wavelength oscillation of Nd laser around 1.3 lm: a potential source for coherent terahertz generation, *Opt. Express*, Vol. 14, Issue 11, 2006, pp. 4721–4726.

[37]. H. Maestre, A. J. Torregrosa, C. R. Fernández-Pousa, M. L. Rico, J. Capmany, Dual-wavelength green laser with a 4.5 THz frequency difference based on self-frequency- doubling in Nd3+-doped aperiodically poled lithium niobate, *Opt. Lett.*, Vol. 33, Issue 9, 2008, pp. 1008–1010.

[38]. G. Shayeganrad, P. Parvin, DIAL–phoswich hybrid system for remote sensing of radioactive plumes in order to evaluate external dose rate, *Progress in Nuclear Energy*, Vol. 51, 2008, pp. 420–433.

[39]. K. A. Fredriksson, DIAL technique for pollution monitoring: improvements and complementary systems, *Appl. Optics*, Vol. 24, Issue 19, 1985, pp. 3297-3304.

[40]. G. Shayeganrad, Single laser-based differential absorption lidar (DIAL) for remote profiling atmospheric oxygen, *Optics and Laser in Engineering*,Vol. 111, 2018, pp. 80-85.

[41]. G. Shayeganrad, On the remote monitoring of gaseous uranium hexafluoride in the lower atmosphere using lidar, *Optics and Lasers in Engineering*, Vol. 51, 2013 pp. 1192–1198

[42]. G. M. Hale, M. R. Querry, Optical constants of water in the 200-nm to 200-μm wavelength region, *Appl. Opt.*, Vol. 12, Issue 3, 1973, pp. 555-563.

[43]. R. Hibst, U. Keller, Experimental studies of the application of the Er:YAG laser on dental hard substances: I. Measurement of the ablation rate, *Lasers in Surgery and Medicine*, Vol. 9, Issue 4, 1989, pp. 338-344.

[44]. E. Kilinc, D. M. Roshkind, S. A. Antonson, D. E. Antonson, P. C. Hardigan, S. C. Siegel, J. W. Thomas, Thermal safety of Er:YAG and Er,Cr:YSGG lasers in hard tissue removal, *Photomedicine and Laser Surgery*, 2009, Vol. 27, Issue 4, pp. 565-570.

[45]. G. M. Peavy, L. Reinisch, J. T. Payne, V. Venugopalan, Comparison of cortical bone ablations by using infrared laser wavelengths 2.9 to 9.2 μm, *Lasers Surg Med.*, Vol. 25, 1999, pp. 421-434.

[46]. M. Ivanenko, R. Sader, S. Afilal, M. Werner, M. Hartschock, C. von Hänisch, S. Amilz, W. Erhardt, H.-F. Zeilhofer, P. Hering, In-vivo animal trials with a scanning CO_2 laser osteotome, *Lasers Surg. Med.*, Vol. 37, Issue 2, 2005, pp. 144-148.

[47]. M. Ivanenko, M. Werner, S. Afilal, M. Klasing, P. Hering, Ablation of hard bone tissue with pulsed CO2 lasers, *Med. Laser Appl.*, Vol. 20, Issue 1, 2005, pp. 13-23.

[48]. C. Parrilla, J. Galli, A. R. Fetoni, M. Rigante, G. Paludetti, Erbium: yttrium-aluminum-garnet laser stapedotomy-A safe technique, *Otolaryngology - Head and Neck Surgery*, Vol. 138, Issue 4, 2008, pp. 507-512.

[49]. T. D. Myers, W. D. Myers, R. M. Stone, First soft tissue study utilising a pulsed Nd:YAG dental laser, *Northwest Dent.*, Vol. 68, Issue 2, 1989, pp. 14-17.

[50]. D. Fried, N. Ashouri, T. Breunig, R. Shori, Mechanism of water augmentation during IR laser ablation of dental enamel, *Lasers Surg. Med.*, Vol. 31, 2002, pp. 186–193.

[51]. Y. Nishimoto, *et al.*, Effect of pulse duration of Er:YAG laser on dentin ablation, *Dent. Mater J.*, 2008, Vol. 27, Issue 3, pp. 433–439.

[52]. M. Hossain, *et al.*, Ablation depths and morpholigical changes in human enamel and dentin after Er:YAG laser irradiation with or without water mist, *Journal of Clinical Laser Medicine & Surgery*, Vol. 17, Issue 3, 1999, pp. 105-109.

[53]. M.-E. Kim, *et al.*, Effects of water flow on dental hard tissue ablation using Er:YAG laser, *Journal of Clinical Laser Medicine & Surgery*, Vol. 21, Issue 3, 2003, pp. 139-144.

[54]. V. Colucci, *et al.*, Water flow on erbium:yttrium–aluminum–garnet laser irradiation: effects on dental tissues, *Laser Med. Sci.*, Vol. 24, Issue 5, 2009, pp. 811-818.

[55]. T. J. Webster, Nanotechnology for the Regeneration of Hard and Soft Tissues, *World Scientific Publishing Co. Pte. Ltd.*, Singapore, 2007.

[56]. J. Woodhead-Galloway, Collagen: The Anatomy of a Protein, *Edward Arnold Limited*, London, 1980.

[57]. E. L. Smith, R. L. Hill, I. R. Lehman, R. J. Lefkowitz, P. Handler, A. White, Principles of Biochemistry: Mammalian Biochemistry, *McGraw-Hill Book Company*, New York, 1983.

[58]. J. J. Pritchard, Bones, *Oxford University Press*, London, 1974.

[59]. V. A. Serebriakov, Laser technologies in medicine, *ITMO*, St. Petersburg, 2009.

[60]. J. Arends, J. L. Ruben, D. Inaba, Major topics in quantitative microradiography of enamel, and dentin: R parameter, mineral distribution visualization, and hyper-remineralization, *Adv. Dent. Res.*, Vol. 11, Issue 4, 1997, pp. 403-414.

[61]. L. Kuscer, J. Diaci, Measurements of erbium laser-ablation efficiency in hard dental tissues under different water cooling conditions, *Journal of Biomedical Optics*, Vol. 18, 2013, p. 108002.

[62]. M. H. Niemz, Laser-Tissue Interactions: Fundamentals and Applications, *Springer-Verlag*, Berlin Heidelberg, 2007.

[63]. C. Garban-Labaune, *et al.*, Effect of Laser Wavelength and Pulse Duration on Laser-Light Absorption and Back Reflection, *Appl. Phys. Lett.*, Vol. 48, 1982, pp. 1018-1021.

[64]. D. Fried, R. E. Glena, J. D. B. Featherstone, W. Seka, Permanent and Transient Changes in the Reflectance of CO2 Laser-Irradiated Dental Hard Tissues at lamda = 9.3, 9.6, 10.3, and 10.6 μm and at Fluences of 1-20 J/cm2, *Lasers in Surgery and Medicine*, Vol. 20, 1997, pp. 22-31.

[65]. S. Alves, V. Oliveira, R Vilar, Femtosecond laser ablation of dentin, *J Phys. D: Appl. Phys.*, Vol. 45, Issue 24, 2012, p. 245401.

[66]. J. Neev, L. B. Da Silva, M. D. Feit, M. D. Perry, A. M. Rubenchik, B. C. Stuart, Ultrashort pulse lasers for hard tissue ablation, *IEEE Journal of Selected Topics in Quantum Electronics*, Vol. 2, 1995, pp. 790-800.

[67]. F. Sanchez, A. J. Espana Tost, J. L. Morenza, ArF excimer laser irradiation of human dentin, *Lasers Surg. Med.*, Vol. 21, 1997, pp. 474–479.

[68]. S. Eugenio, M. Sivakumar, R. Vilar, A. M. Rego, Characterisation of dentin surfaces processed with KrF excimer laser radiation, *Biomaterials*, Vol. 26, 2005, pp. 6780–6787.

[69]. M. J. C. van Gemert, A. J. Welch, Clinical use of laser-tissue interactions, *IEEE Engineering in Medicine and Biology Magazine*, 1989, Vol. 8, Issue 4, pp. 10-13.

[70]. C. V. Gabel, Femtosecond lasers in biology: nanoscale surgery with ultrafast optics, *Contemporary Physics*, Vol. 49, Issue 6, 2008, pp. 391-411.

[71]. S. H. Chung, E. Mazur, Surgical applications of femtosecond lasers, *J. Biophoton*, Vol. 2, Issue 10, 2009, pp. 557-572.

[72]. Q. Feng, Y. N. Picard, H. Liu, S. M. Yalisove, G. Mourou, T. M. Pollock, Femtosecond laser micromachining of a single-crystal superalloy, *Scripta Materialia*, 2005, Vol. 53, Issue 5, pp. 511–516.

[73]. S. Baudach, J. Bonse, W. Kautek, Ablation experiments on polyimide with femtosecond laser pulses, *Appl. Phys. A*, Vol. 69, 1999, pp. S395-S398.

[74]. R. Le Harzic, D. Beritling, M. Weikert, S. Sommer, C. Föhl, S. Valette, C. Donnet, E. Audouard, F. Dausinger, Pulse width and energy influence on laser micromachining of metals in a range of 100 fs to 5 ps, *Appl. Surf. Sci.*, Vol. 249, Issue 1-4, 2005, pp. 322-331.

[75]. Y. Huang, S. Liu, W. Li, Y. Liu, W. Yang, Two-dimensional periodic structure induced by single-beam femtosecond laser pulses irradiating titanium, *Opt. Express*, Vol. 17, 2009, pp. 20756–20761.

[76]. G. Kamlage, T. Bauer, A. Ostendorf, B. N. Chichkov, Deep drilling of metals by femtosecond laser pulses, *Appl. Phys. A: Mater. Sci. Process.*, Vol. 77, Issue 2, 2003, pp. 307-310.

[77]. V. Kara, H. Kizil, Titanium micromachining by femtosecond laser, *Opt. Lasers Eng.*, Vol. 50, 2012, pp. 140-147.

[78]. H. C. Wang, H. Y. Zheng, P. L. Chu, J. L. Tan, K. M. Teh, T. Liu, B. C. Y. Ang, G. H. Tay, Femtosecond laser drilling of alumina ceramic substrates, *Appl. Phys. A: Mater. Sci. Process.*, Vol. 101, 2010, pp. 271-278.

[79]. D. Pietroy, Y. Di Maio, B Moine, E. Baubeau, E. Audouard, Femtosecond laser volume ablation rate and threshold measurements by differential weighing, *Opt. Express*, Vol. 20, Issue 28, 2012, pp. 29900-29908.

[80]. A. Borowiec, H. K. Hangen, Femtosecond laser micromachining of grooves in indium phosphide, *Appl. Phys. A*, Vol. 79, Issue 3, 2004, pp. 521–529.

[81]. D. Stern, *et al.*, Corneal ablation by nanosecond, picosecond, and femtosecond lasers at 532 and 625 nm, *Arch. Ophthalmol.*, Vol. 107, Issue 4, 1989, pp. 587–592.

[82]. H. Chen, J. Liu, H. Li, W. Ge, Y. Sun, Y. Wang, P. Lü, Femtosecond laser ablation of dentin and enamel: relationship between laser fluence and ablation efficiency, *Journal of Biomedical Optics*, Vol. 20, Issue 2, 2015, p. 028004.

[83]. J. Krüger, W. Kautek, H. Newesely, Femtosecond-pulse laser ablation of dental hydroxyapatite and single-crystalline fluoroapatite, *Appl. Phys. A*, 1999, Vol. 69, pp. S403–S407.

[84]. R. F. Z. Lizarelli, M. M. Costa, E. Carvalho-Filho, F. D. Nunes, V. S. Bagnato, Selective ablation of dental enamel and dentin using femtosecond laser pulses, *Laser Phys. Lett.,* Vol. 5, 2008, pp. 63–69.

[85]. G. Shayeganrad, L. Mashhadi, Study of aerosols and molecular extinction effects in ultraviolet DIAL remote sensing in the lower atmosphere, *International Journal of Remote Sensing*, 2012, Vol. 33, pp. 887–904.

[86]. I. M. Vardavas, F. W. Taylor, Radiation and Climate, *Oxford University Press*, 2007.

[87]. A. J. Cox, A. J. DeWeerd, J. Linden, An experiment to measure Mie and Rayleigh total scattering cross sections, *Am. J. Phys.*, Vol. 70, Issue 6, 2002, pp. 620-625.

[88]. M. I. Skolnik, Introduction to radar systems (3rd Ed.), McGraw Hill, Inc., New Delhi, India, 2001.

[89]. Jose P. Peixoto, Oort Abraham H., Physics of Climate, *Springer*, 1992.

[90]. W. S. Benedict, E. K. Plyler, Absorption spectra of water vapor and carbon dioxide in the region of 2.7 microns, *Journal of Research of the National Bureau of Standards*, Vol. 46, Issue 3, 1951, pp. 246-265.

[91]. J. N. Howare, D. L. Burch, D. Williams, Near-infrared transmission through synthetic atmospheres, *Geophys. Res. Papers*, Vol. 40, 1955, p. 244.

[92]. R. M. Goody, Atmospheric Radiation: Theoretical Basis, *Oxford University Press,* 1964.

[93]. S. Arba-Mosquera, D. de Ortueta, Geometrical analysis of the loss of ablation efficiency at non-normal incidence, *Opt. Express*, Vol. 6, 2008, pp. 3877-3895.

[94]. S. Arba-Mosquera, S. Verma, Analytical optimization of the ablation efficiency at normal and non-normal incidence for generic super Gaussian beam profiles, *Biomed. Opt. Express*, Vol. 4, Issue 8, 2013, pp. 1422-1433.

[95]. G. M. Hale, M. R. Querry, Optical Constants of Water in the 200-nm to 200-um Wavelength Region, *App. Opt.*, Vol. 12, Issue 3, 1973, pp. 555-563.

[96]. B. Majaron, B. Sustersic, M. Lukac, U. Skaleric, N. Funduk, Heat diffusion and debris screening in Er:YAG laser ablation of hard biological tissues, *Appli. Phys. B*, Vol. 66, Issue 4, 1998, pp. 479-487.

[97]. T. Perhavec, M. Lukac, J. Diaci, M. Marincek, Heat deposition of erbium lasers in hard dental tissues, *J. Oral Laser Appl*, Vol. 9, Issue 4, 2009, pp. 205-212.

[98]. T. Perhavec, J. Diaci, Comparison of Er:YAG and Er, Cr:YSGG dental lasers, *J. Oral Laser Appl*, Vol. 8, Issue 2, 2008, pp. 87–94.

[99]. M. Lukac, *et al*., Super short VSP Er:YAG pulses for fast and precise cavity preparation, *J. Oral Laser Appl*., Vol. 4, 2004, pp. 171–173.

[100]. B. Majaron, B. Sustersic, M. Lukac, U. Skaleric, N. Funduk, Heat diffusion and debris screening in Er:YAG laser ablation of hard biological tissues, *Appl. Phys. B*, Vol. 66, 1998, pp. 1-9.

[101]. Q. T. Le, R. Vilar, C. Bertrand, Influence of external cooling on the femtosecond laser ablation of dentin, *Lasers Med. Sci*., Vol. 32, Issue 9, 2017, pp. 1943-1951.

[102]. F. J. O. Landa, X. L. Dean-Ben, F. Motero de Espinosa, D. Razansky, Noncontact monitoring of incision depth in laser surgery with air-coupled ultrasound transducers, *Optics Letters*, Vol. 41, Issue 12, 2016, pp. 2704-2707.

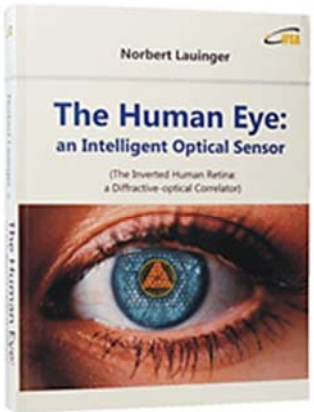
[103]. N. Lukacˇ, T. Suhorrsnik, M. Lukacˇ, and M. Jezerška, Ablation characteristics of quantum square pulse mode dental erbium laser, *Journal of Biomedical Optics*, Vol. 21, Issue 1, 2016, pp. 015012-1–015012-10.

Published by International Frequency Sensor Association (IFSA) Publishing, S. L., 2018 (http://www.sensorsportal.com).

Norbert Lauinger

IFSA

The Human Eye:
an Intelligent Optical Sensor
(The Inverted Human Retina: a Diffractive-optical Correlator)

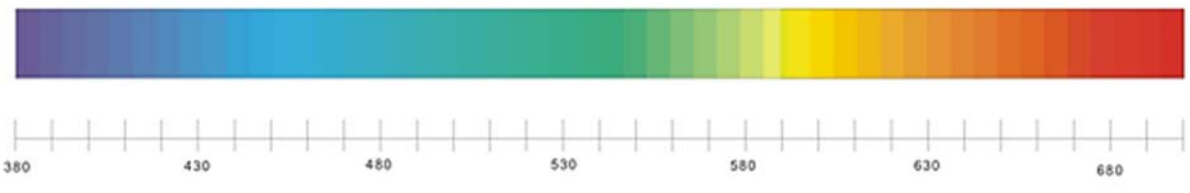


Hardcover: ISBN 978-84-617-2934-0
e-Book: ISBN 978-84-617-2955-5

The Human Eye: an intelligent optical sensor (The inverted retina: a diffractive - optical correlator) shows that the human eye from the prenatal structuring of the inverted retina hardware on up to the design of the central cortical visual pathway is not only different from but also radically more intelligent than a camera.

Many paradoxes in color vision (RGB peak positioning in the visible spectrum, overlapping of the RGB channels, relating local color to the whole scene, paradoxically colored shadows, Purkinje phenomenon etc.) are becoming intelligent solutions.

A fascinating book for all those wondering that the brightness of a scene is not cut in half and that the visible world doesn't collapse into a flat 2D-image when closing one eye. It should be a great of interest for students, scientists and engineers in eye-, vision- and brain-research, neuroscience, psychophysics, ophthalmology, psychology, optical sensor and diffractive optical engineering. Practical applications are the search for a retinal implant of the next generation and a helpful strategy against myopia in early childhood.



Order: http://www.sensorsportal.com/HTML/BOOKSTORE/Human_Eye.htm